

AperTO - Archivio Istituzionale Open Access dell'Università di Torino

Preservation of sub-microscopic structural relicts in micas from the Gran Paradiso Massif (Western Alps): Implications for ^{40}Ar - ^{39}Ar geochronology

This is the author's manuscript

Original Citation:

Availability:

This version is available <http://hdl.handle.net/2318/144687> since

Published version:

DOI:10.1016/j.gca.2013.05.043

Terms of use:

Open Access

Anyone can freely access the full text of works made available as "Open Access". Works made available under a Creative Commons license can be used according to the terms and conditions of said license. Use of all other works requires consent of the right holder (author or publisher) if not exempted from copyright protection by the applicable law.

(Article begins on next page)

PRESERVATION OF SUB-MICROSCOPIC STRUCTURAL RELICS IN MICAS FROM THE GRAN PARADISO MASSIF (WESTERN ALPS): IMPLICATIONS FOR ^{40}Ar - ^{39}Ar GEOCHRONOLOGY

Marco Beltrando^{1*}, Gianfranco Di Vincenzo², Cristiano Ferraris³

¹ Dipartimento di Scienze della Terra, Università di Torino, Via Valperga Caluso 35, 10125 Torino, Italy

² Consiglio Nazionale delle Ricerche, Istituto di Geoscienze e Georisorse, Via Moruzzi 1, 56124 Pisa, Italy

³ Muséum National d'Histoire Naturelle, Laboratoire de Minéralogie et Cosmochimie, 61, Rue Buffon, 75005 Paris, France

*email: marco.beltrando@unito.it

Abstract

Permian igneous biotite and white mica that were re-heated at 500-550°C in the Middle-Late Eocene were investigated by laser step-heating and in-situ ^{40}Ar - ^{39}Ar techniques, in conjunction with scanning electron microscopy (SEM), electron microprobe (EMP) and transmission electron microscopy (TEM) to assess the influence of short-lived metamorphism on K-Ar systematics. Large intra- and inter-grain age variations, ranging from the Triassic to the Late Eocene, are primarily related to the extent of metamorphic re-equilibration. Brown biotite porphyroclasts from weakly re-equilibrated samples are characterized by core-to-rim zoning in major element composition, mineral structure and $^{40}\text{Ar}/^{39}\text{Ar}$ ratios. Titanium concentration and Fe/(Mg+Fe) ratios decrease from crystal cores towards the rims, which are compositionally indistinguishable from green biotite aggregates in metamorphic coronas. Compositional changes are coupled with structural modifications towards the crystal edges, where the disordered igneous $1M$ - $2M_1$ stacks are replaced topotactically by highly ordered metamorphic $1M$ polytypes. Apparent ages up to ~66 Ma were determined in crystal cores by in situ laser-probe analyses, while ages as young as ~45 Ma are typical of crystal rims. Step-heating experiments of these zoned biotites yielded a discordant saddle-shaped age spectrum, with a concordant central segment yielding an error-weighted mean age of 44.9 ± 0.3 Ma. Biotite porphyroclasts from a more re-equilibrated specimen gave markedly different results, with uniform major elements compositional profiles, homogeneous argon distribution throughout the crystals and a flat age spectrum at 36.5 ± 0.3 Ma. TEM investigations of these optically homogeneous porphyroclasts revealed that the original igneous structure had been replaced by highly ordered $1M$ polytypes during Alpine metamorphism. White mica yielded comparable results, with spot ages up to ~218 Ma in domains characterized by high Na/(Na+K) ratios and low Si and Ti content, representing the best preserved igneous relicts. Significantly younger apparent ages, down to 44-39 Ma, are typical of domains affected by partial re-equilibration at high-pressure conditions, as indicated by increasing Si and Ti contents, or by exhumation-related exsolution of amoeboidal quartz. These results indicate that different intra-grain and inter-grain Ar concentration patterns arise primarily from the relative amount and distribution of relict igneous and metamorphic crystal-chemical domains. Core-to-rim age gradients in biotite result from inward-directed recrystallization from the crystal edges, eventually leading to flat age profiles as

metamorphic replacement of pre-existing porphyroclasts runs to completion. This study calls for caution when estimating thermal histories from apparent age gradients or from age vs. grain size correlations, unless the presence of pre-metamorphic mineral relics can be ruled out.

Keywords: ^{40}Ar - ^{39}Ar geochronology, biotite, white mica, TEM, recrystallization

1. Introduction

Geochronological studies conducted in metamorphic terranes have repeatedly shown that Ar concentration within tri- and di-octahedral micas can be markedly heterogeneous. Published patterns include core-to-rim (e.g. Smith et al., 2005) or rim-to-core younging trends (e.g. Pickles et al., 1997) or, more commonly, complex age variations unrelated to crystal edges (e.g. Scaillet et al., 1992; Hodges et al., 1994; Scaillet, 1996; Hames and Cheney, 1997; Giorgis et al., 2000; Kramar et al., 2001; Sherlock and Kelley, 2002; Di Vincenzo et al., 2006; Schneider et al., 2008). Different processes have been proposed to account for the observed age spread, including: (1) thermally activated partial loss of radiogenic argon, dependent upon the distance from crystal edges (Dodson, 1973; Smith et al., 2005) or crystal defects (Hames & Cheney, 1997; Kramar et al., 2001; Mulch and Cosca, 2004; Hames et al., 2008; Cosca et al., 2011); (2) episodic influx of externally derived argon, possibly followed by subsequent diffusional loss (Arnaud & Kelley, 1995; Pickles et al., 1997, Giorgis et al., 2000; Sherlock & Kelley, 2002; Warren et al., 2011); (3) fluid-mediated recrystallization, leading to the local re-equilibration of mica porphyroclasts (Villa, 1998; Di Vincenzo et al., 2001 and 2006; Tartése et al., 2011).

Deciphering the relative contribution of these mechanisms to argon re-distribution within metamorphic minerals has fundamental bearings on the interpretation of ^{40}Ar - ^{39}Ar data and on its use in geo- and thermo-chronology. This task may be complicated by the concomitant occurrence of more than one of the above mechanisms within most metamorphic rocks, which commonly undergo heating-cooling cycles associated with multiple stages of deformation and recrystallization. Therefore, a fair assessment of the mechanisms that controlled Ar re-distribution within a specific rock should include, alongside ^{40}Ar - ^{39}Ar step heating and in-situ analyses, spatially-controlled mineral chemistry and mineral structural data. These different data sets have been combined only in a handful of studies on white mica (e.g. Giorgis et al., 2000; Di Vincenzo et al., 2001), phlogopite (Camacho et al., 2012) and K-feldspar (Villa and Hanchar, 2013).

The study presented here is aimed at investigating the relationship between K-Ar systematics, nano-structural, micro-structural and compositional modifications that affected igneous Permian micas during Tertiary Alpine metamorphism. While this study is mainly focused on biotite, white mica has also been analysed to provide a more complete picture of Ar mobility and availability within the system. The contribution of recrystallization to argon redistribution is assessed with a multi-disciplinary approach

combining laser step-heating and in-situ ^{40}Ar - ^{39}Ar techniques with scanning electron microscopy (SEM), electron microprobe (EMP) and transmission electron microscopy (TEM) analyses.

2. Geological Setting

The Gran Paradiso Massif crops out in the axial zone of the Western Alps (Fig. 1). It is usually grouped together with the Monte Rosa and Dora Maira Massifs under the common label of Internal Crystalline Massifs. It is tectonically overlain by the ophiolitic Eclogitic Piemonte Units and rests tectonically above the Money gneisses, attributed to the Briançonnais domain (Fig. 1). The Gran Paradiso Massif consists of orthogneiss originated from a porphyritic granite intruded at 275-265 Ma (Bertrand et al., 2005; Ring et al., 2005) at $P=0.25\text{-}0.35\text{ GPa}$ (Gabudianu-Radulescu et al., 2011) into a Variscan basement consisting of metapelites and minor meta-mafic rocks (e.g. Callegari et al., 1969; Le Bayon and Ballevre, 2006). Following Mesozoic rifting, leading to the deposition of a locally preserved sedimentary cover (Elter, 1971), the Gran Paradiso Massif underwent Alpine eclogite-facies metamorphism (e.g. Compagnoni and Lombardo, 1974). Metamorphic pressures in excess of 1.8 GPa have been estimated in different lithologies, with local differences possibly reflecting the presence of several sub-units (Le Bayon et al., 2006; Gabudianu Radulescu et al., 2009; Gasco et al., 2010). The orthogneiss generally lacks any evidence of high-pressure mineral assemblages, apart from occasional jadeite (Saliot, 1973). Temperatures $\geq 550^\circ\text{C}$ were reached during exhumation, at $P=0.8\text{-}1.5\text{ GPa}$ (Le Bayon et al., 2006; Gasco et al., 2010). Pervasive re-equilibration under epidote-amphibolite facies conditions was accompanied by the formation of a sub-horizontal fabric, which is characteristically observed in the field. Syn-deformation shear zones in orthogneiss contain quartz, K-feldspar, plagioclase (An_{0-5} and An_{17-27}), biotite, white mica, titanite \pm epidote \pm garnet \pm ilmenite (Menegon and Pennacchioni, 2010). Despite this multi-stage Alpine metamorphic evolution, large areas of the massif completely escaped fabric re-equilibration, preserving mineralogical and textural record of their pre-Alpine evolution (Callegari et al., 1968; Le Bayon and Ballevre, 2006; Menegon and Pennacchioni, 2010; Gabudianu Radulescu et al., 2011).

3. Existing Geochronology

Alpine metamorphism in the Gran Paradiso Massif can be bracketed to the 48-33 Ma interval. The lower boundary at $\sim 48\text{-}44\text{ Ma}$ is provided by tectonic events recorded in the Eclogitic Piemonte Units and in the Briançonnais domain (Fig. 2): the Piemonte ophiolites, originally located in a more distal part of the rifted margin (e.g. Elter, 1972; Beltrando et al., 2010a), underwent Alpine high-pressure metamorphism at 48-44 Ma (e.g. U-Pb on zircon Rubatto et al., 1998; ^{40}Ar - ^{39}Ar on white mica, Beltrando et al., 2009; U-Pb on zircon, Beltrando et al., 2010b); the Briançonnais domain, which belonged to a more proximal part of the

European paleo-margin compared to the Internal Crystalline Massifs, instead, was still lying at the surface in the Lutetian (46-40 Ma), as attested by the deposition of flysch sediments (e.g. Stampfli et al., 1998). Furthermore, Zircon Fission Track ages in the 33-30 Ma range for the Gran Paradiso Massif (Hurford and Hunziker, 1989) and ~29 Ma for the southern Dora Maira Massif (Gebauer et al., 1997) provide a reliable upper limit for the metamorphic evolution (Fig. 2). Indeed, a large number of radioisotopic data for the different stages of Alpine metamorphism in the Internal Crystalline Massifs fall within the interval defined above, generally in the 43-33 Ma range (see Fig. 2 and Rosenbaum and Lister, 2005 and Beltrando et al., 2010a for reviews). High pressure metamorphism has been dated at 42.6 ± 0.6 Ma in the Monte Rosa Massif (U-Pb on rutile; Lapen et al., 2007) and at ~38-35 Ma in the southern Dora Maira Massif [U-Pb on zircon (Tilton et al., 1991; Gebauer et al., 1997), Sm-Nd and Lu-Hf on garnet (Tilton et al., 1991; Duchêne et al., 1997), U-Pb on titanite (Rubatto and Hermann, 2001), Rb-Sr on phengite-whole rock (Di Vincenzo et al., 2006)].

The timing of the different stages of the tectonometamorphic evolution of the Gran Paradiso Massif is somewhat less well defined than in the Monte Rosa and Dora Maira Massifs. Contrasting estimates have been proposed, depending upon the technique and the rock type investigated (Fig. 2). Crystallization of monazite and allanite at high-pressure conditions in talc-chloritoid micaschists has been constrained at 37.4 ± 0.9 Ma and 33.7 ± 1.6 Ma, respectively (U-Pb; Gabudianu-Radulescu et al., 2009). These results are at odds with Rb-Sr estimates of 43.0 ± 0.5 Ma for high-pressure metamorphism in the same rock sample (phengite-apatite; Meffan Main et al., 2005), followed by retrogression at greenschist facies conditions after 36 Ma (phengite-paragonite and paragonite-albite; Meffan Main et al., 2005). Rb-Sr geochronological studies on the Gran Paradiso orthogneiss are broadly consistent with the picture arising from the talc-chloritoid micaschists, as age estimates on deformed orthogneiss usually fall in the 42-33 Ma range (Inger and Ramsbotham, 1997; Rosenbaum et al., 2012). Shear zone activity at $P \geq 1.0$ GPa along the western boundary between the Gran Paradiso Massif and the Piemonte Units has been dated at 41.2 ± 1.1 Ma (Rb-Sr on white mica-epidote-apatite; Rosenbaum et al., 2012). Greenschist facies shear zones bounding the Gran Paradiso Massif to the north and to the east yielded younger estimates at 33.2 ± 0.4 Ma (Rb-Sr on white mica-feldspar; Freeman et al., 1997) and 39-34 Ma (Rb-Sr on white mica-feldspar-epidote; Inger and Ramsbotham, 1997). Importantly, pre-Alpine apparent ages have commonly been reported. Ages of 207.3 ± 2.7 Ma and >80 Ma were estimated in a meta-granitoid largely preserving the original mineral assemblage and texture (Rb-Sr on muscovite-feldspar; Inger and Ramsbotham, 1997) and in a sheared meta-granitoid (Rb-Sr on quartz-feldspar-white mica; Rosenbaum et al., 2012), respectively. As noted in both studies, different white mica grain fractions are characterized by contrasting Sr-isotopic signatures, with larger mica crystals yielding older apparent ages. This feature has been interpreted as evidence for isotopic inheritance and incomplete recrystallisation of the original igneous white mica during Alpine deformation/metamorphism (Inger and Ramsbotham, 1997; Rosenbaum et al., 2012).

143 Similar to Rb-Sr data, ^{40}Ar - ^{39}Ar studies on white mica also yielded a large age spread from ~160 to ~30
144 Ma (Fig. 2; Chopin and Maluski, 1980; Reddy et al., 2003). A narrow range has been found exclusively in
145 phengite from a highly sheared granitoid, with step ages of 44-37 Ma from step-heating experiments
146 (Chopin and Maluski, 1980) and in white mica + biotite aggregates from an epidote-amphibolite shear zone,
147 yielding apparent ages in the 40-36 Ma range (Rosenbaum et al., 2012). More commonly, step-heating
148 experiments resulted in highly discordant age spectra, with pre-Alpine apparent ages up to ~65 Ma in
149 metagranites (Chopin and Maluski, 1980) and in the 120-40 Ma range in a sheared meta-pelite (Rosenbaum
150 et al., 2012). Importantly, in the latter example coarser-grained mineral separates yielded older apparent
151 ages. Furthermore, apparent ^{40}Ar - ^{39}Ar ages in the 77-30 Ma range are characteristic of biotite-white mica
152 aggregates from samples where isotopic inheritance was inferred from Rb-Sr data (samples GP03-163 and
153 GP03-161 in Rosenbaum et al., 2012). In the Teleccio Lake area, where the samples that are the subject of
154 this study were collected, several steps of previous step-heating experiments yielded apparent ages
155 between ~80 and ~40 Ma (Rosenbaum et al., 2012). Differently from white mica, biotite has rarely been the
156 focus of geochronological studies: apparent ages in the 31-27 Ma range have been reported for partly
157 chloritized relics of magmatic biotite (Chopin and Maluski, 1980), while K-Ar dating of magmatic biotite
158 yielded 45 ± 1 Ma (Krommenacher and Evernden, 1970).

159 In summary, syn-kinematic mineral assemblages from different rock types generally yielded apparent
160 ages in the 44-33 Ma range (Fig. 2). However, largely undeformed meta-granites and, occasionally, sheared
161 orthogneisses, yielded older ages, when analysed by both Rb-Sr and ^{40}Ar - ^{39}Ar techniques. These ages were
162 initially believed to indicate the timing of Alpine high pressure metamorphism (Chopin and Maluski, 1980),
163 but have subsequently been tentatively related to an excess argon component (Reddy et al., 2003) or,
164 alternatively, to the preservation of pre-Alpine mineral relics partly re-equilibrated during the Alpine
165 orogenic cycle (Inger and Ramsbotham, 1997; Rosenbaum et al., 2012). The study presented here aims at
166 addressing this controversy, testing whether pre-Alpine ^{40}Ar - ^{39}Ar ages may be related to incomplete re-
167 setting of the pre-existing mineral reservoirs in biotite and white mica.

168

169

170 **4. Petrographic Description**

171 Samples were collected along the banks of the Teleccio Lake. Details on the pre-Alpine and Alpine
172 tectonometamorphic evolution of this small area, where Compagnoni and Lombardo (1974) reported the
173 first evidence of Alpine eclogites in the Gran Paradiso Massif, can be found in an extensive body of
174 literature (e.g. Compagnoni and Lombardo, 1974; Le Goff and Ballevre, 1990; Menegon and Pennacchioni,
175 2010; Gabudianu Radulescu et al., 2011; Rosenbaum et al., 2012). Two meta-granitoids, characterized by
176 the best preserved igneous assemblage (JT1007) and by the partial static re-equilibration of the original
177 igneous assemblage, without the formation of a new Alpine fabric (JT1008), were selected.

178 Sample JT1007 is a meta-granite, with a well preserved igneous assemblage consisting of quartz + K-
179 feldspar + plagioclase + biotite and accessory apatite, zircon and monazite (Fig. 3a and Supplementary Fig.
180 1). This sample is coarse grained, with sub-centimeter sized quartz and K-feldspar. The latter commonly
181 displays Karlsbaab twinning and exsolutions along the cleavage planes. Igneous plagioclase, often
182 preserving polysynthetic twinning, is generally zoned, with crystal rims of oligoclase composition and cores
183 largely replaced by fine-grained aggregates consisting of albite + white mica + zoisite. Brown biotite (Bt1) is
184 usually found in aggregates of millimeter to pluri-millimeter sized crystals, often associated with apatite
185 and zircon inclusions, surrounded by the characteristic dark halo (Fig. 3b). The igneous mineral assemblage
186 is partly re-equilibrated as a result of Alpine metamorphism, as indicated by coronitic mineral assemblages.
187 Bt1 is frequently rimmed by thin fine-grained aggregates of white mica + ilmenite (Fig. 3c), locally replaced
188 by a second rim of green biotite (Bt2) + titanite. Ilmenite is common both along the edges of Bt1 crystals
189 and along the cleavage planes. When Bt2 aggregates are directly in contact with Bt1 porphyroclasts (Fig.
190 3b), igneous brown biotite displays a weak zoning towards the green-brown rims. Further evidence of
191 Alpine re-equilibration include epidote rims around magmatic monazite, albite + white mica + zoisite
192 aggregates formed at the expense of the cores of magmatic plagioclase, albite + white mica aggregates
193 along the edges of magmatic K-feldspar and rare chlorite replacing biotite. Minor evidence of Alpine
194 deformation is restricted to occasional kinking of the igneous biotite and to the local development of
195 subgrains along the edges of large quartz crystals, which display weak wavy extinction (Fig. 3a).

196 Sample JT1008 is a two-mica tourmaline-bearing meta-aplite, with an original mineral assemblage
197 consisting of medium grained K-feldspar + plagioclase + biotite + white mica + quartz, with accessory
198 tourmaline, apatite and zircon (Supplementary Fig. 1). The main differences with respect to JT1007 concern
199 the extent of Alpine re-equilibration. Pluri-millimeter sized magmatic quartz is rare, being generally
200 replaced by medium- to fine-grained aggregates of quartz crystals with lobated margins and wavy
201 extinction, often preserving the original crystallographic orientation of the parent crystal (Fig. 3d). Brown
202 biotite relics are locally kinked and are commonly surrounded by coronas of ilmenite + medium sized white
203 mica (Wm2; ~100 μm in diameter; Fig. 3e). Rare rutile is observed both associated with Wm2 and along the
204 cleavage planes of igneous biotite. Ilmenite + Wm2 aggregates are then locally replaced by green biotite
205 (Bt2) + titanite. Green biotite aggregates, occasionally hosting white mica (Wm3) are common around Bt1
206 (Fig. 3f). Small crystals of igneous biotite may be completely replaced by Bt2 aggregates. Chlorite is very
207 rarely observed to replace small Bt1 crystals.

208 Igneous pluri-mm white mica crystals (Wm1), often kinked (Figs. 3f and 3g), are common in this
209 sample. When in contact with igneous biotite, they are generally overgrown by rims consisting of ilmenite +
210 Wm2 in optical continuity with Wm1 (Fig. 3f). Patchy re-equilibration of Wm1 is indicated by a number of
211 petrographic observations, including crystallographically-unrelated variations in back-scattered electron
212 (BSE) emission (Fig. 3g), due to different Ti contents (see below) and the presence of amoeboidal quartz

exsolutions elongated along cleavage planes (Fig. 3h). Furthermore, green biotite (Bt2) or ilmenite are observed both along kink walls and cleavage planes of large Wm1 crystals, which are also occasionally overgrown by albite (Fig. 3i).

5. Mineral chemistry

Mineral chemistry was determined with a JEOL JXA-8200 electron microprobe at the Dipartimento di Scienze della Terra, Università degli Studi di Milano (Italy). Conditions of analyses were 15 kV and 5 nA, and natural standards were employed. Spot sizes were 5 μm for white mica and feldspars and 1 μm for biotite. Representative analyses of biotite and white mica are listed in Table 1 and 2.

Igneous brown biotite and metamorphic green biotite from both samples differ mainly for the Ti content (Figs. 4 a, 4b and 4c). This difference is especially noticeable in JT1007 biotite, where Ti contents of 0.14-0.17 and 0.07-0.10 atoms per formula unit (a.p.f.u.) have been determined for Bt1 and Bt2, respectively (Fig. 4a). Other compositional differences include F content in JT1007, typically in the 0.02-0.07 a.p.f.u. range for Bt1, while it is invariably <0.02 a.p.f.u. in Bt2 (Fig. 4b) and the Mg/(Mg+Fe) ratio in JT1008, where Bt2 is slightly more Mg-rich than Bt1 (Fig. 4c). No significant variation in the Mg/(Mg+Fe) ratio has been detected in JT1007.

Compositional profiles across relict igneous biotite revealed important differences between the two samples (see Figs. 3b, 3e and Supplementary Fig. 2 for the location of the different profiles). Igneous biotite from JT1007 is typically zoned, with mineral composition of the crystal rims converging towards the composition of adjacent green biotite (Figs. 4a, 4b, 4d and 4e). The width of these domains, which are typically green-brown under the optical microscope (Fig. 3b), appears to correlate with the presence of Alpine mineral phases in the specific micro-site. Re-equilibrated areas extend for $\sim 80 \mu\text{m}$ in Bt1 crystals surrounded by abundant Bt2 and/or white mica + ilmenite rims (Figs. 4d and 4e), while they are nearly absent in domains that escaped metamorphic re-equilibration at the microscale (Fig. 4f). Compositional profiles of biotites from JT1008 are instead remarkably homogeneous, even for domains directly adjacent to green biotite aggregates (Figs. 4g, 4h and 4i).

Igneous and metamorphic white mica can be distinguished based on marked compositional differences (Fig. 5). The paragonite component is significantly higher in Wm1 [$\text{Na}/(\text{Na}+\text{K}) \sim 0.1$] than in Wm2 [$\text{Na}/(\text{Na}+\text{K}) \sim 0.02-0.05$]. Furthermore, alpine white mica displays a higher celadonitic component, with silica content in the 3.10-3.22 a.p.f.u. range, as opposed to the values of 3.05-3.09 typical of the igneous white mica (Wm1). The compositional plots shown in Fig. 5 also reveal that Wm1 displays a continuous range of composition from Na-rich, Ti-poor end members, typical of large crystals, to Na-poor and Ti-rich compositions. The latter compositional end member is typical of smaller crystals of igneous white mica adjacent to igneous biotite. BSE images of large Wm1 crystals reveal a rather complex Ti zoning, which

appears to be primarily controlled by the presence of kink walls and the proximity of Bt1. Higher Ti contents (0.05-0.1 a.p.f.u.) are also characteristic of alpine white mica formed in optical continuity with igneous white mica at the expense of igneous biotite. These domains are also characterized by higher Si, Fe and Mg and lower Al than the original Wm1, as typically observed for the celadonitic substitution $(\text{Mg,Fe})^{\text{VI}} + \text{Si}^{\text{IV}}$ for $\text{Al}^{\text{VI}} + \text{Al}^{\text{IV}}$. A rather large compositional range is characteristic of alpine white mica (Fig. 5). Alpine white micas from JT1007 generally fall within the same compositional range as those analysed in JT1008, albeit towards the low-Ti end (Fig. 5).

6. Transmission Electron Microscopy

Biotite crystals from both samples were investigated by TEM (see the Supplementary Material for details of the analytical methods). The two samples yielded significantly different results, consistent with different extent of metamorphic re-equilibration of the two specimens during the Alpine orogeny. Biotite from sample JT1008 is generally homogeneous and mainly consists of a $1M$ polytype, with rare stacking faults (Figs. 6a and 6b). Minor chloritization of the $1M$ biotite is generally restricted to the crystal edges (Figs. 7a and 7b), probably indicating a late-stage metamorphic overprint. Biotite from sample JT1007 is structurally more complex than JT1008 biotite. Core-to-rim structural and chemical zoning is common. Crystal cores display several features that are indicative of crystallization under plutonic conditions (e.g. Fregola and Scandale, 2011), including the reflections with $k \neq 3n$ in Selected Area Electron Diffraction (SAED) patterns, showing streaking typical of stacking disorder (Fig. 6d). In this central portion the $1M$ polytype sequence is rare and sometimes appears alternated to the more common $2M_1$ polytype (Fig. 6c). No evidence of chloritization is found within these biotite relics. Crystal edges are statistically Ti- and Fe-poorer compared to nucleus relics, as also apparent from electron microprobe analyses. This compositional difference is accompanied by a major structural change, as peripheral areas of biotite porphyroclasts consist mainly of the $1M$ polytype. Chloritization is locally observed.

In summary, the structural analyses performed on biotite from both samples indicates that they were affected by Alpine metamorphic recrystallization to different extents. Relics of the original igneous structure are preserved exclusively within cores of the porphyroclasts from sample JT1007. Metamorphic recrystallization resulted in the complete replacement of the igneous structure in JT1008 and in the crystal rims of biotite from sample JT1007.

7. ^{40}Ar - ^{39}Ar geochronology

7.1 Step-heating analyses

Details of the analytical methods for the ^{40}Ar - ^{39}Ar analyses are in the Supplementary Material. Infrared laser step-heating experiments on biotite separates from the two samples gave contrasting results (Figs. 7a and 7b): JT1008 yielded a flat spectrum, for more than 90% of the released $^{39}\text{Ar}_K$, with an error-weighted mean age of 36.5 ± 0.3 Ma; JT1007 yielded a slightly saddle-shaped profile, with initial steps in the 48-52 Ma range followed by a concordant central segment (75% of released $^{39}\text{Ar}_K$), with an error-weighted mean age of 44.9 ± 0.3 Ma. A slight increase of apparent ages to 46-48 Ma is again characteristic of the last 3 steps, which comprise <6% of the total released $^{39}\text{Ar}_K$.

White mica from JT1008 yielded a highly discordant age profile, with most step ages falling in the 79 to 104 Ma range (Fig. 7c). Step 3 yielded the lowest apparent age of 63.4 ± 5.0 Ma, followed by a progressive increase to an age maximum of ~ 129 Ma (step 7). Steps 10 to 18, with the exception of step 12, are characterized by rather constant apparent ages, within the 83-76 Ma range, comprising >26 % of the total $^{39}\text{Ar}_K$.

7.2 In-situ analyses on single grains

Millimeter-sized single crystal separates of JT1007 biotite (Figs. 8a and 8b) and JT1008 white mica (Figs. 8c, 8d and 8e) were also analyzed in situ, to directly image potential age gradients within individual crystals. All analyses were performed on the basal cleavage and they revealed significant intra-grain and inter-grain variations in apparent ages. The best example of intra-grain age variations is provided by a biotite crystal with a diameter >1mm, preserving the original igneous crystallographic shape (Fig. 8a). A broad core-to-rim age gradient is immediately apparent, with the oldest age of 66.1 ± 1.0 Ma in the crystal core and apparent ages consistently <50 Ma along the rims (minimum age is 45.2 ± 0.9 Ma). Importantly, core-to-rim age gradients are not constant, as revealed by a closer inspection of Fig. 8a. Another smaller crystal (Fig. 8b), affected by a larger extent of Alpine re-equilibration, as indicated by minor aggregates of white mica, is characterized by a narrower age spread, from 44.5 ± 0.6 Ma to 51.4 ± 0.7 Ma. Significantly, there is no correlation between apparent age and position within the crystal.

Large intra-grain and inter-grain variations in apparent ages are also typical of white micas (Figs. 8c, 8d and 8e). The relationship between apparent ages and position with respect to crystal core and rim is often difficult to assess, since original crystal edges can be determined only for euhedral crystals. However, being white mica probably a late-crystallizing mineral phase in the igneous protolith, the original crystal edges were often difficult to be detected in the mineral separate. Therefore, only crystallographically controlled crystal edges have been outlined in Figs. 8c, 8d and 8e. Despite these limitations, it is immediately apparent that broad core-to-rim age gradients are characteristic of the analyzed white micas.

318 Apparent ages older than 200 Ma were repeatedly obtained within crystal cores, which yielded ~218 Ma as
319 the oldest age (Fig. 8c). The youngest apparent age of 53.6 ± 2.4 Ma was determined from a
320 crystallographically controlled mineral edge (Fig. 8c). Neighboring sites, only a few hundred micrometers
321 apart, normally yielded widely different apparent ages, with the notable exception of the crystal shown in
322 Fig. 8e, where three analyses performed at relative distances of 0.3-0.5 mm yielded similar ages, in the 90-
323 85 Ma range.

324 Therefore, laser in-situ dating on single crystal separates indicate that both JT1007 biotite and
325 JT1008 white mica are characterized by a very heterogeneous distribution of ^{40}Ar . Although a general
326 decrease of apparent ages toward the rim is observed, $^{40}\text{Ar}^*$ concentration gradients cannot be considered
327 concentric. Occasionally, single crystals yielded a narrower age spread, with most apparent ages
328 comparable to those characteristic of the flat portion of the step-heating age profiles (cfr. Figs. 8b and 8e
329 with Figs. 7a and 7c).

330

331 7.3 In-situ analyses on thick section

332 In-situ analyses on polished rock chips of sample JT1008 were performed to investigate both the
333 spatial distribution of argon isotopes in biotite and the relationship between composition and apparent
334 ages in white mica, which could not be assessed on the single crystal separates.

335 Ten Infrared laser spot analyses were performed on different parts of biotite relics (Bt1), including
336 crystal core, rims and kinked domains. All ages are statistically indistinguishable, ranging from 34.5 ± 1.3
337 Ma to 37.0 ± 1.7 Ma (Figs. 8g and 8h and Supplementary Fig. 3), with an error-weighted mean age of $35.5 \pm$
338 0.5 Ma (MSWD=0.73) for the ten analyses. Two analyses, which yielded slightly older apparent ages (in
339 italic in Table 3 and in Fig. 8) were excluded from the mean calculation because the laser pit also sampled
340 white mica, as apparent from BSE imaging (Fig. 8g) and from the chemical correlation diagram (age vs.
341 $^{38}\text{Ar}_{\text{Cl}}/^{39}\text{Ar}_{\text{K}}$ in Supplementary Fig. 3). Detection of contamination by white mica is based upon the its lower
342 Cl content compared to biotite (Table 1 and 2), resulting in lower Cl/K ratios estimated from neutron-
343 produced Ar isotopes (Supplementary Fig. 3).

344 Seven analyses were performed on a large white mica crystal, with a diameter of ~0.9 mm and with
345 the basal cleavage oriented nearly parallel to the section surface (Fig. 8f and Supplementary Fig. 3). Internal
346 inhomogeneity within this igneous relict is indicated by several observation on the BSE image, including (1)
347 the presence of discrete bright linear domains, consisting of ilmenite along kink walls, with variable spacing
348 in the range of 100-160 μm , (2) the 'porous' appearance of specific domains, due to small quartz
349 exsolutions (Figs. 3g and 3h) and (3) the marked brightness contrast between Ti-rich and Ti-poor domains.
350 Note that the distribution of kink walls, quartz or Ti-enriched mica does not correlate in a simple way with
351 the position within the crystal. No core-to-rim age gradients are found and apparent ages range widely
352 from 128.2 ± 3.3 to 41.7 ± 2.0 Ma, with the two extremes located less than 50 μm apart (Fig. 8f). More

353 significantly, the youngest age was estimated near the crystal core, but comparable apparent ages <50 Ma
354 were also found near the crystal edges. Importantly, the two oldest ages (128.2 ± 3.3 and 79.3 ± 1.8 Ma)
355 were obtained in the only sites that do not cross kink walls and display the lowest BSE emission (Fig. 8f).

356 Another Wm1 crystal, with the basal plane oriented roughly perpendicular to the section surface
357 and located less than 1 mm from the larger crystal described above, was also analysed (Fig. 8g and 8h).
358 Quartz exsolutions, alpine biotite and fine-grained alpine white micas are common within this
359 microstructural domain (Figs. 8g and 8h). An apparent age of 43.8 ± 1.6 Ma was obtained from a domain
360 with abundant quartz exsolutions and minor Alpine biotite (Fig. 8h). A trench spanning the transition area
361 between the Wm1 crystal and a fine-grained aggregate of Wm2 + rare biotite yielded a younger apparent
362 age of 40.8 ± 1.2 Ma. An even younger age of 34.8 ± 1.4 Ma was obtained for the fine-grained aggregate of
363 white mica and biotite (Fig. 8h).

364

365

366 8. Discussion

367

368 8.1 Relationship between crystal-chemical reservoirs and apparent ages

369 Results from the present study document significant inter-grain and intra-grain variations of
370 apparent ages in relict igneous biotite and white mica that underwent an Alpine metamorphic cycle, which
371 culminated with eclogite facies metamorphism under conditions of $P \geq 2.0$ GPa and $T = 500\text{--}550^\circ\text{C}$ (Fig. 8).
372 Similar age variations in other metamorphic terranes have been ascribed to diffusional loss of radiogenic
373 ^{40}Ar from pre-existing sheet silicates (e.g. Hodges et al., 1994; Kramar et al., 2001; Hames et al., 2008).
374 However, in the samples studied here, different crystal-chemical domains can be distinguished within both
375 biotite and white mica relics, based on a combination of petrographic observations (Fig. 3), EMP (Figs. 4 and
376 5) and TEM analyses (Fig. 6), hinting at a potential link between metamorphic re-equilibration and Ar age
377 variations. The apparent age of the different crystal-chemical reservoirs obtained by in-situ laser analyses
378 or step-heating experiment can be assessed either with chemical correlation diagrams (e.g. Villa et al.,
379 2000) or with a tight compositional control on the spatial distribution of the reservoirs (e.g. Giorgis et al.,
380 2000; Di Vincenzo et al., 2006). In the studied samples, the different generations of igneous and
381 metamorphic biotite and white mica in sample JT1007 do not differ significantly and systematically in their
382 Cl and Ca content (Table 1 and 2), thus preventing the use of chemical correlation diagrams. However,
383 compositional profiles, calibrated with nano-structural analyses, provide a consistent picture as to the
384 relative distribution of the two crystal-chemical sites. As a result, the relationships between intra-grain
385 variations in $^{40}\text{Ar}^*$ concentrations and specific crystal-chemical reservoirs can be unravelled.

386

387

8.1.1 Biotite

Two different crystal-chemical sites can be distinguished in porphyroclastic biotite. They are related to the original igneous structure, with disordered stacking of 2M₁ and 1M polytypes, and to metamorphic re-equilibration, resulting into a highly order structure consisting of 1M polytypes. While the igneous structure has been totally erased in JT1008 biotite, which consists entirely of 1M polytypes (Figs. 6a and 6b), biotite from JT1007 is zoned, with igneous nano-structures widely preserved and 1M polytypes restricted to crystal rims (Figs. 6c and 6d). Areas characterized by different polytypes display distinctive compositions, with higher Ti contents and lower Mg/(Mg+Fe) ratios typically associated with the igneous structure. A similar decrease in Ti content between relict igneous biotite and Alpine biotite has already been documented in other high-pressure orthogneisses (e.g. Biino and Compagnoni, 1992). Our TEM study provides new evidence supporting this earlier suggestion. EMP compositional profiles also display a marked Ti decrease and a slight Mg/(Mg+Fe) increase towards the crystal edges, generally restricted to the outermost 80-100 µm, providing a useful tool to assess the relative distribution of igneous structural relicts and newly formed metamorphic biotite (Fig. 4). Importantly, slightly irregular compositional patterns are characteristic of biotite cores (Fig. 4), suggesting that smaller scale structural re-equilibration may also be partly affecting areas that are not directly located along the crystal edges. These deviations may be controlled, at least partly, by the presence of kink walls, which are commonly observed with the optical microscope (Supplementary Fig. 2).

Differently from sample JT1007, biotites from sample JT1008 underwent complete nano-structural re-equilibration during Alpine metamorphism, despite preserving the brown color and the crystal size of the former igneous biotite (Fig. 3e and Supplementary Fig. 2). Compositional profiles are invariably flat, with only minor compositional variations, possibly suggesting that more than one biotite generation may be present, albeit locally (Fig. 4). The different structural and compositional characteristics of the two samples are closely matched by the distribution of in situ laser probe Ar data (Table 3 and Fig. 8g) and by the shape of the step-heating age profiles (Fig. 7b). Biotite from JT1008, which is compositionally and structurally homogeneous as a result of Alpine metamorphism, yielded both a flat age spectrum with an error-weighted mean age of 36.5 ± 0.3 Ma (Fig. 7b) and homogeneous intra-grain Ar concentrations (Fig. 8g). Apparent ages determined by in-situ analyses are statistically indistinguishable, ranging between 34.5 ± 1.3 Ma and 37.0 ± 1.7 Ma (Fig. 9). Biotite from the better preserved JT1007 is instead characterized by a discordant age spectrum, with a significantly older error-weighted mean age of 44.9 ± 0.3 Ma (Fig. 7a) and by significant core-to-rim age variations (Fig. 8a). Apparent ages as old as ~66 Ma were estimated in a crystal core, with a progressive decrease to ~45 Ma at the crystal edge.

Therefore, the results from sample JT1007 and JT 1008 indicate that there is a strong spatial correlation between structural/compositional re-equilibration assessed by EMP and TEM analyses and apparent ^{40}Ar - ^{39}Ar ages. Complete resetting of the argon clock was achieved only in the biotites from

423 JT1008, which underwent thorough nano-structural re-equilibration during Alpine metamorphism, despite
424 preserving the brown color and the crystal size of the pre-existing igneous biotite. The age spread observed
425 in the least re-equilibrated biotites, instead, is best explained as related to the coexistence of two different
426 argon reservoirs tied to the two different structural and compositional sites identified within biotites. A
427 larger relative contribution of the magmatic biotite relics results in geologically meaningless ages >60 Ma,
428 while Eocene ages are related to a larger relative contribution of mineral reservoirs formed during Alpine
429 metamorphism. Different degassing behavior of the two compositionally distinct crystal-chemical reservoirs
430 may be responsible for the slightly discordant age spectrum, as widely documented for mixtures of
431 different generations of white mica (e.g. Wijbrans and McDougall, 1986; Di Vincenzo et al., 2006; Beltrando
432 et al., 2009), amphibole (e.g. Villa et al., 2000; Di Vincenzo and Palmeri, 2001) and possibly biotite (Berger,
433 1975; Maluski, 1978; Dallmeyer, 1982; York and Martinez, 1986).

434

435 8.1.2 *White mica*

436 Petrographic observations and electron microprobe analyses reveal that three main chemical
437 reservoirs can be distinguished within relict igneous white mica. Compositional relicts of the original
438 igneous muscovite, characterized by relatively high Na/(Na+K) and low BSE emissions are occasionally
439 overgrown epitactically by phengitic mica at the contact with adjacent brown biotite (Figs. 3f and 3h). BSE
440 imaging reveals that igneous muscovite hosts Si, Mg, Fe and Ti rich domains extending irregularly within the
441 relict crystals. This compositional change, mainly controlled by the celadonitic substitution $(\text{Mg,Fe})^{\text{VI}} + \text{Si}^{\text{IV}}$ for
442 $\text{Al}^{\text{VI}} + \text{Al}^{\text{IV}}$, is largely related to the presence of kinks or brown biotite nearby. Importantly, chemically re-
443 equilibrated domains are in optical continuity with the igneous muscovite, suggesting that phengitic
444 substitution occurred topotactically. Subsequent re-equilibration is apparent in discrete domains hosting
445 amoeboidal quartz, generally elongated along the basal plane of micas (Fig. 3h). Similar quartz exsolutions
446 in white mica from meta-granitoids of the Dora Maira Massif originated from breakdown of Si-rich
447 phengitic mica into quartz + Si-poor phengite, with rare talc detected exclusively with TEM observations
448 (Ferraris et al., 2000). We suggest that the white micas from the Gran Paradiso Massif record a similar
449 petrographic evolution. Therefore, quartz-rich domains within the sites of the original igneous mica are
450 interpreted as areas that underwent early re-equilibration under HP conditions and subsequent
451 exhumation-related re-equilibration.

452 As already noted above, the three different crystal-chemical sites are distributed irregularly within
453 mica porphyroclasts. The apparent ages obtained with the in-situ laser probe technique on thick section
454 also vary widely, but correlate with the crystal-chemical sites. The oldest apparent ages of ~128 Ma were
455 obtained in areas preserving the least re-equilibrated igneous muscovite (Fig. 8f). Younger apparent ages
456 are instead associated with Ti- and Si-enriched sites (Fig. 8f). The irregular boundaries between the
457 different micro-chemical sites and the size of UV laser pits (300x100 μm) prevented sampling of single

crystal-chemical sites. However, the youngest apparent ages in the 47.0 ± 1.6 to 41.7 ± 2.0 Ma range were estimated from domains hosting the largest relative percentage of the amoeboidal quartz-rich mica. Younger ages of 40.8 ± 1.2 Ma and 34.8 ± 1.4 Ma were determined for domains characterized by variable amounts of fine-grained, newly formed white mica and biotite (Fig. 8h). Therefore, we suggest that the intra-grain age spread from ~ 128 Ma to ~ 42 Ma within white mica porphyroclasts resulted from variable mixing between a pre-Alpine argon reservoir, associated with the igneous relics, and two distinct Alpine reservoirs, related to HP metamorphism and subsequent decompression. Older apparent ages up to ~ 218 Ma have been obtained by in-situ analyses on single crystal separates (Fig. 8c). Therefore, this age can be considered as the minimum apparent age of the argon reservoir associated with the igneous mica relic, while the age of 41.7 ± 2.0 Ma provides an estimate for the maximum timing of formation of the youngest crystal-chemical reservoir, during decompression (Fig. 9a). Once again, the highly discordant spectrum resulting from the step-heating experiment on white mica separate (Fig. 7c) reflects the different degassing behavior of the three crystal-chemical reservoirs identified within relict white mica porphyroclasts.

8.2 Effects of partial argon pressure at the crystal edges

As discussed above, the studied biotites and white micas yielded apparent ages pre-dating the timing of Alpine metamorphism, despite having undergone re-heating at $T \geq 550^\circ\text{C}$. Similar results from other metamorphic terranes have been alternatively ascribed to incomplete diffusional loss or to the episodic intake of extraneous argon from the rock matrix during the metamorphic cycle. However, a significant role of the latter process can be excluded for the Gran Paradiso samples, based on several lines of evidence. Firstly, occurrences of extraneous argon intake within pre-existing sheet silicates commonly result in a rim-to-core decrease of apparent ages (e.g. Pickles et al., 1997; Di Vincenzo et al., 2007; Warren et al., 2011), i.e. opposite to what has been documented for JT1007 biotite and JT1008 white mica. Furthermore, newly formed crystals are more prone to the intake of extraneous argon, as implied by metamorphic white mica and biotite yielding apparent ages older than pre-existing sheet silicates (Arnaud and Kelley, 1995). However, in the examples documented here, texturally younger white mica and biotite invariably yielded younger apparent ages with respect to the igneous relics.

It has been argued that unexpectedly old ages may also arise from non-zero argon concentration at the grain boundaries during metamorphism, slowing down diffusion of argon away from the crystal lattice (e.g. Wheeler, 1996; Kelley and Wartho, 2000). Partial argon pressure may result either from extraneous argon or from the progressive accumulation of radiogenic ^{40}Ar along the crystal edges, in the absence of fast fluid migration pathways (e.g. Kelley, 2002). The presence of non-zero Ar concentrations along the grain boundaries during specific stages of the tectonometamorphic evolution is very difficult to assess with independent evidence, as fluids can be consumed/produced through subsequent mineral reactions (e.g., Proyer, 2003) or removed from the system. However, these processes should affect minerals from a single

specimen equally, unless obvious heterogeneities (i.e. veins) are present. However, the studied samples lack any evidence of metamorphic veining and white micas and biotites of similar grain size display very different apparent age distributions (Figs. 8a, 8b, 8c, 8d and 8e). This pattern is more compatible with locally variable metamorphic re-equilibration, as apparent from petrographic and compositional analyses. Furthermore, the homogeneous ages of JT1008 biotite suggest that, at least at the timing of biotite recrystallization, $^{40}\text{Ar}^*$ stored within pre-existing white mica reservoirs was being removed efficiently from the system. Therefore, we conclude that the measured age gradients in white mica are not the result of local hindrance to diffusion of Ar away from the crystal lattice.

8.3 Argon re-distribution in biotite and white mica during short-lived metamorphism

Our study supports previous evidence from the Gran Paradiso Massif on the preservation of pre-Alpine radiogenic Sr and Ar in large igneous white mica relics in meta-granitoids (Inger and Ramsbotham, 1997; Rosenbaum et al., 2012). These previous suggestions, which can now be confidently extended to biotite, are here substantiated by detailed structural information by TEM analyses for biotite and by in-situ laser probe geochronology on both white mica and biotite. Therefore, argon loss from the studied igneous micas heated up to $T \geq 550^\circ\text{C}$ was primarily controlled by metamorphic re-equilibration, rather than volume diffusion. It is worth noting that the preservation of apparent ages up to ~ 216 Ma in white mica with a diameter of ~ 1.2 mm (Fig. 8c) from the Gran Paradiso Massif is not surprising, as it is in accordance with the argon diffusivity determined experimentally for white mica (Harrison et al., 2009). In principle, the observations presented in this study do not allow excluding that the observed age pattern in white mica resulted from the interplay of volume diffusion from the igneous reservoirs combined with episodic re-crystallization.

On the other hand, the preservation of pre-Alpine ages in igneous biotite is incompatible with experimentally determined Ar diffusivity for biotite (Harrison et al., 1985; Grove and Harrison, 1996), which predicts complete diffusive loss from millimeter-sized crystal flakes at the metamorphic temperature reached by the Gran Paradiso Massif. Anomalously old apparent ages have already been reported in several studies (e.g. Villa and Puxeddu, 1994; Kelley et al., 1997; Kelley and Wartho, 2000; Maurel et al., 2003). These results have been alternatively interpreted as indicating that biotite is significantly more retentive than commonly assumed (Villa and Puxeddu, 1994; Maurel et al., 2003) or ascribed to high Ar concentration along the grain boundaries, slowing down diffusional loss from the mica crystal (Kelley et al., 1997; Kelley and Wartho, 2000), or attributed to < 1 Myr heating-cooling cycles (Lister and Baldwin, 1996). In the case presented here, the pre-Alpine ages are specifically tied to igneous crystal-chemical relicts, while they are absent in Alpine crystal-chemical sites, supporting the view that Ar mobility in the studied biotite was lower than predicted by experimental studies. In principle the Cretaceous ages estimated for the crystal cores might alternatively result from mixing between igneous and metamorphic micro-

528 reservoirs, from partial argon loss from the igneous reservoir only, or from a combination of both
529 processes. The different scales of observations adopted in this study, ranging from $\sim 0.01 \mu\text{m}^2$ for the
530 nanostructural analysis by TEM, to $1\text{--}25 \mu\text{m}^2$ for compositional analyses by EMP to $10000\text{--}30000 \mu\text{m}^2$ for in-
531 situ geochronology prevent clarifying this latter aspect. Despite these limitations, the significant
532 discrepancy between measured and predicted ages suggests caution when applying experimentally
533 determined diffusion parameters to naturally heated biotite.

534 Most importantly, the study presented here suggests that, in the absence of detailed mineral
535 structure data, great caution should be taken when estimating the thermal history of metamorphic rocks
536 from $^{40}\text{Ar}^*$ concentration profiles, under the assumption that Ar mobility is primarily controlled by volume
537 diffusion. The study on relict biotite from sample JT1008 shows that flat age spectra and homogeneous Ar
538 distribution, rather than resulting from complete argon loss during Alpine heating, arose from complete
539 recrystallization of the pre-existing brown biotite crystal. Importantly, detection of this process may escape
540 inspection by optical microscopy and, possibly, compositional determinations by EMP. On the other hand,
541 apparent core-to-rim age variations of the kind detected in biotite from JT1007 may be the result of
542 incomplete recrystallization, rather than reflect incomplete diffusional loss. Therefore, in specific
543 circumstances 'diffusion profiles' might be an artifact due to variable mixing of two distinct sub-microscopic
544 argon reservoirs.

545 The presence of compositionally distinct argon reservoirs, likely characterized by different
546 degassing behavior during the step-heating experiments, is also responsible for the discordant age spectra
547 resulting from the step-heating experiments on mineral separates (Figs. 7a and 7c). Saddle-shaped age
548 spectra of the kind obtained from JT1007 biotite might, in principle, arise for the presence of extraneous
549 argon (e.g. Harrison and McDougall, 1981) or the input of melt and fluid inclusions (Esser et al., 1997;
550 Boven et al., 2001). The study presented here, instead, shows that an older gas reservoir, rather than being
551 related to externally-derived ^{40}Ar , is microstructurally tied to igneous crystal-chemical relics.

552 Another important feature emerging from this study, which may deserve future research, is related
553 to the broad correlation between crystal size, Alpine re-equilibration and apparent ages observed in
554 specific micro-sites. Compositional analyses, combined with petrographic observations, showed that
555 smaller crystals are generally more prone to undergo metamorphic re-equilibration (see the 'large' and
556 'small' white micas in Fig. 5) and therefore be affected by loss of previously accumulated $^{40}\text{Ar}^*$ (cfr. Figs. 8f
557 and 8h). This process results into a broad correlation between crystal size and apparent age. Similar
558 relationships have been reported for pre-orogenic micas that underwent subduction/orogeny-related
559 metamorphism (e.g. Goodwin and Renne, 1991; Lo and Onstott, 1995; Reddy et al., 1996). Our study
560 suggests caution when using this type of data to estimate diffusion parameters in mica or cooling rates of
561 metamorphic terranes, unless the presence of multiple reservoirs of the kind documented here can be

ruled out, as correlations between crystal size and apparent age may reflect different extents of metamorphic re-equilibration, rather than different diffusion length scales.

8.4 Geological significance of the measured ages

Crystallization ages in the 44-33 Ma range have generally been provided for syn-kinematic mineral assemblages from the Gran Paradiso Massif (see 'Geological Setting'). However, the presence of undetected mineral relics of the kind documented here might skew Rb-Sr and ^{40}Ar - ^{39}Ar data towards ages pre-dating the metamorphic/deformation event of interest. Biotite from sample JT1008 yielded very consistent results (Fig. 9) and an error-weighted mean age of 36.5 ± 0.3 Ma can be calculated from the step-heating experiment. Due to the compositional and structural homogeneity of the dated biotites, which have been completely transformed into 1M metamorphic polytypes, this age is interpreted to date the re-crystallization event. Metamorphic biotite within the original igneous biotite site is compositionally very similar to green biotite found in the rock matrix, in equilibrium with low-Si white mica and titanite. Therefore, the age of 36.5 ± 0.3 Ma is interpreted to constrain post-HP re-equilibration, during exhumation. The lack of direct relationships with albite and zoisite, which are also found as late metamorphic minerals in JT1008, does not allow defining whether green biotite formed under greenschist facies conditions or during the previous epidote-amphibolite facies metamorphic stage. Despite these limitations, our estimates suggest that the Gran Paradiso Massif was at relatively low-P conditions at 36.5 ± 0.3 Ma. This estimate is in accordance with the zircon fission track ages of 33-30 Ma (Hurford and Hunziker, 1989), while it is barely within error (2σ) with respect to the U-Pb age of 33.7 ± 1.6 Ma for allanite provided by Gabudianu-Radulescu et al. (2009), which probably underestimates the timing of HP metamorphism. We note that the error-weighted mean ages of 36.5 ± 0.3 and 35.5 ± 0.5 Ma estimated from the step-heating experiment and the in-situ laser probe analyses, respectively, do not overlap within 2σ errors. This slight difference may be explained by a larger extent of chloritization of the biotites that have been dated in situ with respect to those separated and hand-picked for the step-heating experiment. Indeed, minor chlorite interlayering has been imaged by TEM (Fig. 6). Any other specific geological inference from the geochronological data presented in this study should be taken with care, as all apparent ages from biotite in JT1007 and white mica in JT1008 should be considered as mixed ages.

9. Conclusions

This multi-disciplinary investigation of white mica and biotite shows that pre-metamorphic K-bearing minerals might preserve at least part of their radiogenic argon despite having undergone re-heating at $T \geq 550^\circ\text{C}$. In this context, different patterns of intra-grain variations in Ar concentration may result primarily from the relative distribution of relict and metamorphic crystal chemical sites. Progressive recrystallization

597 from the edges towards crystal cores may result in core-to-rim age gradients within single crystals.
598 Complete replacement of pre-existing porphyroclasts during metamorphism, instead, may lead to flat
599 compositional profiles. Irregular recrystallization, partly unrelated to crystallographic edges, which is more
600 likely in deformed and/or larger crystals, results in patchy age patterns. None of these age patterns should
601 be interpreted as resulting from volume diffusion alone. Therefore, in metamorphic rocks, care should be
602 taken when extrapolating thermal histories from argon data, unless the presence of pre-metamorphic
603 mineral relics can be ruled out.

604

605

606 **Acknowledgments**

607 M.B. acknowledges the financial support of the Margin Modelling 3 consortium. R. Compagnoni is thanked
608 for discussions. A. Risplendente provided assistance with the EMP analyses and G. De Grandis helped with
609 the mineral separation.

610

611

612

613 **References:**

614 Arnaud N. O. and Kelley S. P. (1995) Evidence for excess argon during high pressure metamorphism
615 in the Dora Maira massif (Western Alps, Italy) using an ultra-violet laser ablation microprobe ^{40}Ar - ^{39}Ar
616 technique. *Contrib. Mineral. Petrol.* **121**, 1–11.

617 Baronnet A. (1992) Polytypism and stacking disorder. In *Minerals and reactions at the atomic scale:*
618 *transmission electron microscopy* (Ed. P.R. Buseck). Mineralogical Society of America, Washington DC, Rev.
619 Mineral. 27, pp. 231–288.

620 Baronnet A. (1997) Equilibrium and kinetic processes for polytype and polysome generation. In
621 *Modular Aspects of Minerals* (Ed S. Merlino). EMU Notes in Mineralogy, Budapest, 1, pp. 119–152.

622 Baronnet A., Nitsche S. and Kang Z.C. (1993) Layer stacking microstructures in a biotite single crystal:
623 a combined HRTEM-AEM study. *Phase Transition* **43**, 107–128.

624 Beltrando M., Lister G., Forster M., Dunlap W.J., Fraser G. and Hermann J. (2009) Dating
625 microstructures by the ^{40}Ar - ^{39}Ar step-heating technique: deformation–Pressure–Temperature–time history
626 of the Penninic Units of the Western Alps. *Lithos* **113**, 801–819.

627 Beltrando M., Compagnoni R. and Lombardo B. (2010a) (Ultra-) High-pressure metamorphism and
628 orogenesis: An Alpine perspective. *Gondwana Research* **18**, 147–166, doi:10.1016/j.gr.2010.01.009

629 Beltrando M., Rubatto D. and Manatschal G. (2010b) From passive margins to orogens: The link
630 between Ocean-Continent Transition zones and (Ultra-)High-Pressure metamorphism. *Geology* **38**, 559–
631 562, doi:10.1130/G30768.1

632 Berger G.W. (1975) ^{40}Ar – ^{39}Ar step heating of thermally overprinted biotite, hornblende and
633 potassium feldspar from Eldora, Colorado. *Earth Planet. Sci. Lett.* **26**, 387–408.

634 Bertrand J.M., Paquette J.L. and Guillot F. (2005) Permian zircon U–Pb ages in the Gran Paradiso
635 massif: revisiting post- Variscan events in the Western Alps. *Schweiz. Mineral. Petrogr. Mitt.* **85**, 15–29.

636 Boven A., Pasteels P., Kelley S.P., Punzalan L., Bingen B. and Demaiffe D. (2001) $^{40}\text{Ar}/^{39}\text{Ar}$ study of
637 plagioclases from the Rogoland anorthosite complex (SW Norway); an attempt to understand argon ages in
638 plutonic plagioclase. *Chem. Geol.* **176**, 105–135.

639 Callegari E., Compagnoni R. and Dal Piaz G.V. (1969) Relitti di strutture intrusive erciniche e scisti a
640 sillimanite nel Massiccio del Gran Paradiso. *Boll. Soc. Geol. It.* **88**, 59–69.

641 Camacho A., Lee J., Fitzgerald J., Zhao J., Abdu Y.A., Jenkins D.M., Hawthorne F.C., Kyser T.K.,
642 Creaser R.A., Armstrong R., Heaman L.W. (2012) Planar defects as Ar traps in trioctahedral micas: A
643 mechanism for increased Ar retentivity in phlogopite. *Earth Planet. Sci. Lett.* **341–344**, 255–267.

644 Chopin C. and Maluski H. (1980) ^{40}Ar – ^{39}Ar dating of high-pressure metamorphic micas from the Gran
645 Paradiso area (Western Alps): evidence against the blocking temperature concept. *Contrib. Mineral. Petrol.*
646 **74**, 109–122.

647 Compagnoni R. and Lombardo B. (1974) The Alpine age of the Gran Paradiso eclogites. *Rend. Soc. It.*
648 *Min. Petrol.* **30**, 220–237.

649 Cosca M., Stunitz H., Bourgeix A.L. and Lee J.P. (2011) $^{40}\text{Ar}^*$ loss in experimentally deformed
650 muscovite and biotite with implications for $^{40}\text{Ar}/^{39}\text{Ar}$ geochronology of naturally deformed rocks. *Geochim.*
651 *Cosmochim. Acta* **75**, 7759–7778.

652 Dallmeyer R.D. (1982) $^{40}\text{Ar}/^{39}\text{Ar}$ incremental-release ages of biotite from a progressively
653 remetamorphosed Archean basement terrane in southwestern Labrador. *Earth Planet. Sci. Lett.* **61**, 85–96.

654 Di Vincenzo G. and Palmeri R. (2001) An ^{40}Ar – ^{39}Ar investigation of high–pressure metamorphism
655 and the retrogressive history of mafic eclogite from the Lanterman Range (Antarctica): evidence against a
656 simple temperature control on Ar transport in amphibole. *Contrib. Mineral. Petrol.* **141**, 15–35.

657 Di Vincenzo G., Ghiribelli B., Giorgetti G. and Palmeri R. (2001) Evidence of a close link between
658 petrology and isotope records: constraints from SEM, EMP, TEM and in situ ^{40}Ar – ^{39}Ar laser analyses on
659 multiple generations of white micas (Lanterman Range, Antarctica). *Earth Planet. Sci. Lett.* **192**, 389–405.

660 Di Vincenzo G., Tonarini S., Lombardo B., Castelli D. and Ottolini L. (2006) Comparison of ^{40}Ar – ^{39}Ar
661 and Rb–Sr data on phengites from the UHP Brossasco–Isasca Unit (Dora Maira massif, Italy): implications
662 for dating white mica. *J. Petrol.* **47**, 1439–1465.

663 Dodson M. H. (1973) Closure temperature in cooling geochronological and petrological systems:
664 *Contrib. Mineral. Petrol.* **40**, 259–274.

665 Duchêne S., Blichert-Toft J., Luais B., Télouk P., Lardeaux J.M. and Albarède F. (1997) The Lu–Hf
666 dating of garnets and the ages of the Alpine high-pressure metamorphism. *Nature* **387**, 586–589.

667 Elter G. (1971) Schistes lustrés et ophiolites de la zone piémontaise entre Orco et Doire Baltée
668 (Alpes graies). *Géologie Alpine* **47**, 147–169.

669 Elter G. (1972) Contribution a la connaissance du Briançonnais interne et de la bordure piémontaise
670 dans les Alpes Graies nord-orientales et considérations sur les rapports entre les zones du Briançonnais et
671 des Schistes Lustrés. *Ist. Geol. Mineral. Univ. Padova Mem.* **28**, 19 pp.

672 Esser R.P., McIntosh W.C., Heizler M.T. and Kyle P.R., 1997. Excess argon in melt inclusions in zero-
673 age anorthoclase feldspar from Mt Erebus, Antarctica, as revealed by the $^{40}\text{Ar}/^{39}\text{Ar}$ method. *Geochim.*
674 *Cosmochim. Acta* **61**, 3789–3801.

675 Ferraris C., Chopin C. and Wessicken R. (2000) Nano to microscale decompression products in
676 ultrahigh-pressure phengite: HRTEM and AEM study, and some petrological implications. *Am. Mineral.* **85**,
677 1195–1201.

678 Freeman S.R., Inger S., Butler R.W.H. and Cliff R.A. (1997) Dating deformation using Rb–Sr in white
679 mica: greenschist facies deformation ages from the Entrelor shear zone, Italian Alps. *Tectonics* **16**, 55–76.

680 Gabudianu Radulescu I., Rubatto D., Gregory C. and Compagnoni R. (2009) The age of HP
681 metamorphism in the Gran Paradiso Massif, Western Alps: a petrological and geochronological study of
682 “silvery micaschists”. *Lithos* **110**, 95–108.

683 Gabudianu Radulescu I., Compagnoni R. and Lombardo B. (2011) Polymetamorphic history of a
684 relict Permian hornfels from the central Gran Paradiso Massif (Western Alps, Italy): a microstructural and
685 thermodynamic modelling study. *J. metamorphic Geol.* **29**, 851–874, 10.1111/j.1525-1314.2011.00943.x

686 Gasco I., Borghi A. and Gattiglio M. (2010) Metamorphic evolution of the Gran Paradiso Massif: a
687 case study of an eclogitic metagabbro and a polymetamorphic glaucophane– garnet micaschist. *Lithos* **115**,
688 101–120.

689 Gebauer D., Schertl H.P., Brix M. and Schreyer W. (1997) 35 Ma old ultrahigh-pressure
690 metamorphism and evidence for very rapid exhumation in the Dora Maira Massif, Western Alps. *Lithos* **41**,
691 5–24.

692 Giorgis D., Cosca M.A. and Li S. (2000) Distribution and significance of extraneous argon in UHP
693 eclogite (Sulu terrain, China): insights from in situ $^{40}\text{Ar}/^{39}\text{Ar}$ UV-laser ablation analysis. *Earth Planet. Sci. Lett.*
694 **181**, 605–615.

695 Goodwin L.B. and Renne P.R. (1991) Effects of progressive mylonitization on Ar retention in biotites
696 from the Santa Rosa mylonite zone, California, and thermochronologic implications. *Contrib. Mineral.*
697 *Petrol.* **108**, 283–297.

698 Grove M. and Harrison T.M. (1996) $^{40}\text{Ar}^*$ diffusion in Fe-rich biotite. *Am. Min.* **81**, 940–951.

699 Hames W.E. and Cheney J.T. (1997) On the loss of $^{40}\text{Ar}^*$ from muscovite during polymetamorphism.
700 *Geochim. Cosmochim. Acta* **61**, 3863–3872.

701 Hames W. E., Cheney J. T. and Tracy R. J. (2008). Single-crystal $^{40}\text{Ar}/^{39}\text{Ar}$ age variation in muscovite
 702 of the Gassetts Schist and associated gneiss, Vermont Appalachians. *Am. Mineral.* **93**, 384–395.

703 Harrison T.M. and McDougall I. (1981) Excess ^{40}Ar in metamorphic rocks from Broken Hill, New
 704 South Wales: implications for $^{40}\text{Ar}/^{39}\text{Ar}$ age spectra and the thermal history of the region. *Earth Planet. Sci.*
 705 *Lett.* **55**, 123–149.

706 Harrison T.M., Duncan I. and McDougall I. (1985) Diffusion of ^{40}Ar in biotite: Temperature, pressure
 707 and compositional effects. *Geochim. Cosmochim. Acta* **49**, 2461–2468.

708 Harrison T.M., Célérier J., Aikman A.B., Hermann J. and Heizler M.T. (2009) Diffusion of ^{40}Ar in
 709 muscovite. *Geochim. Cosmochim. Acta* **73**, 1039–1051.

710 Hodges K.V., Hames W.E. and Bowring S.A. (1994) $^{40}\text{Ar}/^{39}\text{Ar}$ age gradients in micas from a high
 711 temperature-low pressure metamorphic terrain: evidence for very slow cooling and implications for the
 712 interpretation of age spectra. *Geology* **22**, 55–58.

713 Hurford A. J. and Hunziker J.C. (1989) A revised thermal history for the Gran Paradiso massif.
 714 *Schweiz. Mineral. Petrogr. Mitt.* **69**, 319–329.

715 Inger S. and Ramsbotham W. (1997) Syn-convergent exhumation implied by progressive
 716 deformation and metamorphism in the Valle dell'Orco transect, NW Italian Alps. *J. Geol. Soc. London* **154**,
 717 667–677.

718 Kelley S.P., Bartlett J.M. and Harris N.B.W. (1997) Pre-metamorphic ages from biotite inclusions in
 719 garnet. *Geochim. Cosmochim. Acta* **61**, 3873–3878.

720 Kelley S. (2002) Excess argon in K–Ar and Ar–Ar geochronology. *Chem Geol.* **188**, 1–22. doi:
 721 10.1016/S0009-2541(02)00064-5.

722 Kelley S.P. and Wartho J.-A. (2000) Rapid kimberlite ascent and the significance of Ar–Ar Ages in
 723 xenolith phlogopites. *Science* **289**, 609–611.

724 Kramar N., Cosca M.A. and Hunziker J.C. (2001) Heterogeneous $^{40}\text{Ar}^*$ distributions in naturally
 725 deformed muscovite: in-situ UV-laser ablation evidence for microstructurally controlled diffusion. *Earth*
 726 *Planet. Sci. Lett.* **192**, 377–388.

727 Krummenacher D. and Evernden J.F. (1960) Déterminations d'âge isotopique faites sur quelques
 728 roches des Alpes par la méthode potassium-argon. *Schweiz. Mineral. Petrogr. Mitt.* **40**, 267–277.

729 Lapen T.J., Johnson C.M., Baumgartner L.P., Dal Piaz G.V., Skora S. and Beard B.L. (2007) Coupling of
 730 oceanic and continental crust during Eocene eclogite-facies metamorphism: evidence from the Monte Rosa
 731 nappe, western Alps. *Contrib. Mineral. Petrol.* **153**, 139–157.

732 Le Bayon B. and Ballèvre M. (2006) Deformation history of a subducted continental crust (Gran
 733 Paradiso, Western Alps): continuing crustal shortening during exhumation. *J. Struct. Geol.* **28**, 793–815.

734 Le Goff E. and Ballèvre M. (1990) Geothermobarometry in albite-garnet orthogneisses: a case of
 735 study from the Gran Paradiso nappe (Western Alps). *Lithos* **25**, 261–280.

736 Lister G.S. and Baldwin S.L. (1996) Modelling the effect of arbitrary P–T–t histories on argon
 737 diffusion in minerals using the MacArgon program for the Apple Macintosh. *Tectonophysics* **253**, 83–109.

738 Lo C.H. and Onstott T.C. (1995) Rejuvenation of K–Ar systems for minerals in the Taiwan mountain
 739 belt. *Earth Planet. Sci. Lett.* **131**, 71–98.

740 Maluski H. (1978) Behaviour of biotites, amphiboles, plagioclases K-feldspars in response to
 741 tectonic events with the ^{40}Ar – ^{39}Ar radiometric method. Example of Corsican granite. *Geochim. Cosmochim.*
 742 *Acta* **42**, 1619–1633.

743 Maurel O., Monié P., Respaut J.P., Leyreloup A.F. and Maluski H. (2003) Pre-metamorphic ^{40}Ar – ^{39}Ar
 744 and U–Pb ages in HP metagranitoids from the Hercynian belt (France). *Chem. Geol.* **193**, 195–214,
 745 doi:10.1016/S0009-2541(02) 00351-0.

746 Meffan-Main S., Cliff R.A., Barnicoat A.C., Lombardo B. and Compagnoni R. (2004) A tertiary age for
 747 Alpine high-pressure metamorphism in the Gran Paradiso massif, Western Alps: a Rb–Sr microsampling
 748 study. *J. metamorph. Geol.* **22**, 267–281.

749 Menegon L. and Pennacchioni G. (2010) Local shear zone pattern and bulk deformation in the Gran
 750 Paradiso metagranite (NW Italian Alps). *Int. J. Earth Sci.* **99**, 1805–1825.

751 Mulch A. and Cosca M. (2004) Recrystallization or cooling ages: in situ UV-laser $^{40}\text{Ar}/^{39}\text{Ar}$
 752 geochronology of muscovite in mylonitic rocks. *J. Geol. Soc. London* **161**, 573–582.

753 Pickles C.S., Kelley S.P., Reddy S.M. and Wheeler J. (1997) Determination of high spatial resolution
 754 argon isotope variations in metamorphic biotites. *Geochim. Cosmochim. Acta* **61**, 3809–3824.

755 Proyer A. (2003) The preservation of high-pressure rocks during exhumation: metagranites and
 756 metapelites. *Lithos* **70**, 183–194.

757 Reddy S.M., Kelley S.P. and Wheeler J. (1996) A $^{40}\text{Ar}/^{39}\text{Ar}$ laser probe study of micas from the Sesia
 758 Zone, Italian Alps: implications for metamorphic and deformation histories. *J. metamorph. Geol.* **14**, 493–
 759 508.

760 Reddy S.M., Wheeler J., Butler R.H.W., Cliff R.A., Freeman S., Inger S., Pickles C. and Kelley S.P.
 761 (2003) Kinematic reworking and exhumation within the convergent Alpine Orogen. *Tectonophysics* **365**, 77–
 762 102.

763 Ring U., Collins A.S. and Kassem O.K. (2005) U–Pb SHRIMP data on the crystallization age of the
 764 Gran Paradiso augengneiss, Italian Western Alps: further evidence for Permian magmatic activity in the Alps
 765 during break-up of Pangea. *Eclogae geol. Helv.* **98**, 363–370.

766 Rosenbaum G. and Lister G.S. (2005) The Western Alps from the Jurassic to Oligocene: spatio-
 767 temporal constraints and evolutionary reconstructions. *Earth Sci. Rev.* **69**, 281–306.

768 Rosenbaum G., Menegon L., Glodny J., Vasconcelos P., Ring U., Massironi M., Thiede D. and
 769 Nasipuri P. (2012) Dating deformation in the Gran Paradiso Massif (NW Italian Alps): Implications for the
 770 exhumation of high-pressure rocks in a collisional belt. *Lithos* **144–145**, 130–144.

771 Rubatto D., Gebauer D. and Fanning M. (1998) Jurassic formation and Eocene subduction of the
 772 Zermatt–Saas–Fee ophiolites: implications for the geodynamic evolution of the Central and Western Alps.
 773 *Contrib. Mineral. Petrol.* **132**, 269–287.

774 Rubatto D. and Hermann J. (2001) Exhumation as fast as subduction? *Geology* **29**, 3–6.

775 Saliot P. (1973) Les principales zones de métamorphisme dans les Alpes françaises. Répartition et
 776 signification. *Comptes rendus de l'Académie des Sciences (Paris)* **276**, 3081–3084.

777 Scaillet S., Féraud G., Lagabriele Y., Ballèvre M. and Ruffet G. (1990) $^{40}\text{Ar}/^{39}\text{Ar}$ laser-probe dating by
 778 step heating and spot fusion of phengites from the Dora Maira nappe of the western Alps, Italy. *Geology*
 779 **18**, 741–744.

780 Scaillet S., Feraud G., Ballèvre M. and Amouric M. (1992) Mg/Fe and [(Mg/Fe)Si–Al₂] compositional
 781 control on argon behaviour in high-pressure white micas: a $^{40}\text{Ar}/^{39}\text{Ar}$ continuous laser-probe study from the
 782 Dora–Maira nappe of the internal western Alps, Italy. *Geochim. Cosmochim. Acta* **56**, 2851–2872.

783 Scaillet S. (1996) Excess ^{40}Ar transport, scale and mechanism in high-pressure phengites – a case-
 784 study from an eclogitized metabasite of the Dora-Maira nappe, Western Alps. *Geochim. Cosmochim. Acta*
 785 **60**, 1075–1090.

786 Schneider J., Bosch D. and Monié P. (2008) Individualization of textural and reactional
 787 microdomains in eclogites from the Bergen Arcs (Norway): Consequences for Rb/Sr and Ar/Ar
 788 radiochronometer behavior during polymetamorphism. *Geochem. Geophys. Geosyst.* **9**, Q12001,
 789 doi:10.1029/2008GC002098.

790 Sherlock S. and Kelley, S. (2002) Excess argon evolution in HP-LT rocks: A UVLAMP study of phengite
 791 and K-free minerals, NW Turkey. *Chem. Geol.* **182**, 619–636, doi:10.1016/S0009-2541(01)00345-X.

792 Smith S.R., Kelley S.P., Tindle A.G. and Breaks F.W. (2005) Compositional controls on $^{40}\text{Ar}/^{39}\text{Ar}$ ages
 793 of zoned mica from a rare-element pegmatite. *Contrib. Mineral. Petrol.* **149**, 613–626, doi:10.1007/s00410-
 794 005-0674-7

795 Stampfli G.M., Mosar J., Marquer D., Marchant R., Baudin T. and Borel G. (1998) Subduction and
 796 obduction processes in the Swiss Alps. *Tectonophysics* **296**, 159–204.

797 Tartèse R., Ruffet G., Poujol M., Boulvais P. and Ireland T.R. (2011) Simultaneous resetting of the
 798 muscovite K–Ar and monazite U–Pb geochronometers: a story of fluids. *Terra Nova* **23**, 390–398. doi:
 799 10.1111/j.1365-3121.2011.01024.x

800 Tilton G.R., Schreyer W. and Schertl H.P. (1991) Pb–Sr–Nd isotopic behaviour of deeply subducted
 801 crustal rocks from the Dora Maira Massif, Western Alps, Italy — II: what is the age of the ultrahigh-pressure
 802 metamorphism? *Contrib. Mineral. Petrol.* **108**, 22–33.

803 Villa I.M. (1998) Isotopic closure. *Terra Nova* **10**, 42–47.

804 Villa I. M. (2010) Disequilibrium textures vs equilibrium modelling: geochronology at the
 805 crossroads. *Geol. Soc. London Spec. Publ.* **332**, 1–15.

806 Villa I.M. and Puxeddu M. (1994) Geochronology of the Larderello geothermal field: new data and
 807 the “closure temperature” issue. *Contrib. Mineral. Petrol.* **115**, 415–426.

808 Villa I.M., Hermann J., Muentener O. and Trommsdorff V. (2000) ^{39}Ar – ^{40}Ar dating of multiply zoned
 809 amphibole generations (Malenco, Italian Alps). *Contrib. Mineral. Petrol.* **140**, 363–381.

810 Villa I.M. and Hanchar J.M. (2013) K-feldspar hygrochronology. *Geochim. Cosmochim. Acta* **101**, 24–
 811 33.

812 York D. and Lopez Martinez M. (1986) The two-faced mica. *Geophys. Res. Lett.* **9**, 973–975.

813 Warren C., Sherlock S. and Kelley S. (2011) Interpreting high-pressure phengite $^{40}\text{Ar}/^{39}\text{Ar}$ laserprobe
 814 ages: an example from Saih Hatat, NE Oman. *Contrib. Mineral. Petrol.* **161**, 991–1009. doi: 10.1007/s00410-
 815 010-0576-1.

816 Wheeler J. (1996) Diffarg: a program for simulating argon diffusion profiles in minerals. *Computers*
 817 *& Geosciences* **22**, 919–929, doi: 10.1016/S0098-3004(96)00061-1.

818 Wijbrans J.R. and McDougall I. (1986) $^{40}\text{Ar}/^{39}\text{Ar}$ dating of white micas from an Alpine high pressure
 819 metamorphic belt on Naxos (Greece): the resetting of the argon isotopic system. *Contrib. Mineral. Petrol.*
 820 **93**, 187–194.

821
 822
 823 Figure captions:

824
 825 Fig. 1: simplified tectonic map of the Gran Paradiso Massif (modified from Gabudianu Radulescu et al.,
 826 2011). Star indicates sampling location. 1 = Gran Paradiso orthogneiss; 2 = Gran Paradiso micaschists; 3 =
 827 Gran Paradiso meta-volcanics; 4 = Money gneiss; 5 = Briançonnais domain; 6 = Piemonte units; 7 = Sesia
 828 Zone.

829
 830 Fig. 2: selected geochronological data from the Gran Paradiso Massif subdivided according to rock type and
 831 dating technique. References: [1] Gabudianu Radulescu et al., 2009; [2] Meffan Main et al., 2004; [3] Inger
 832 and Ramsbotham, 1997; [4] Rosenbaum et al., 2012; [5] Freeman et al., 1997; [6] Chopin and Maluski,
 833 1980. Only steps comprising >1% of the total ^{39}Ar released from Rosenbaum et al. (2012) and Chopin and
 834 Maluski (1980) have been plotted. Ms=micaschist

835
 836 Fig. 3: photomicrographs and SEM images of the samples selected for $^{40}\text{Ar}/^{39}\text{Ar}$ geochronology. The original
 837 igneous texture and mineral size are well preserved in sample JT1007 (a), where brown biotite
 838 porphyroclasts are locally rimmed by metamorphic coronas of green-brown biotite (b). Older metamorphic
 839 coronas also consist of phengitic white mica + ilmenite (c). In JT1008 igneous quartz is completely replaced
 840 by polycrystalline aggregates (d) and brown biotite is partly replaced by metamorphic coronas consisting of

841 phengitic mica + ilmenite or green-brown biotite and muscovite (e). Phengitic mica also crystallizes
842 epitactically around igneous white mica (Wm1), at the expense of brown biotite (f). Igneous white mica is
843 variably recrystallized, depending upon the presence of kink walls and the crystal size (g, h; note that the
844 brightness contrast is related to variable Ti-content. Dashed orange line marks areas with abundant quartz
845 exsolutions. See text for details). Late-stage albite is locally forming at the expense of white mica (i)

846

847 Fig. 4: mineral chemistry data from the different biotite generations in JT1007 and JT1008. Compositional
848 profiles of brown biotite porphyroclasts are shown in (d), (e), (f) for sample JT1007 and (g), (h), (i) for
849 sample JT1008. Analysed crystals are shown in Fig. 3 and Supplementary Fig. 2.

850

851 Fig. 5: mineral chemistry data for the different white mica generations in JT1007 and JT1008.

852

853 Fig. 6: (a) Low magnification TEM image of sample JT1008. This sample is mainly a 1M polytype as for the
854 SAED in the figure inset. Minor chloritization is indicated by the brighter areas parallel to the stacking,
855 perpendicular to c^* . This chlorite layers are more evident in (b) where a TEM high resolution image shows
856 how 14 Å thick chlorite (chl) layers enter the 10 Å biotite structure. (c) [110] HRTEM image of disordered
857 biotite (Bt1) found within JT1007 cores. The stacking vectors (0, +, -) are indicated (Baronnet 1992, 1997;
858 Baronnet et al., 1993). The presence of disordered biotite polytypes is confirmed by streaks in the SAED
859 patterns (d).

860

861 Fig. 7: age release spectra of biotite from sample JT1007 and biotite and white mica from sample JT1008.

862

863 Fig. 8: in-situ age data. Line drawings show the distribution of laser-spot analyses in single crystal separates
864 of JT1007 biotite (a, b) and JT1008 white mica (c, d, e). Red lines indicate crystallographically controlled
865 mineral edges in white mica. SEM images and laser pits in the thick section of JT1008 (f, g, h). Yellow
866 rectangles indicate UV pits, while brown lines define the edges of multiple IR shots. Dashed brown lines
867 indicate IR pits that have been excluded from the calculation of the error-weighted mean age for biotite
868 due to contamination by white mica, as apparent both from the SEM image and the measured ^{38}Ar (CI)
869 content (see Supplementary Fig. 3). Analysed sites falling outside the field of view can be seen on
870 Supplementary Fig. 3.

871

872 Fig. 9: synthesis of the geochronological estimates from white mica and biotite. Steps of the step-heating
873 experiments are plotted individually. The timing of crystallization of the igneous protolith is taken from
874 Bertrand et al. (2005) and Ring et al. (2005). Estimates of high pressure metamorphism in the Piemonte

875 units is from Rubatto et al. (1998), Beltrando et al. (2009), Beltrando et al. (2010b). Zircon Fission Track
876 data from the Gran Paradiso Massif is from Hurford and Hunziker (1989)

877
878 Table 1: representative electron microprobe analyses of the studied biotites.

879
880 Table 2: representative electron microprobe analyses of the studied white micas.

881
882 Table 3: in situ and step-heating ^{40}Ar - ^{39}Ar data. Argon isotope concentrations are in V. IR= infrared laser;
883 UV= ultraviolet laser. Steps of the step-heating experiments used to calculate the error-weighted mean age
884 are in bold characters.

885
886

Table 1

Sample	JT1007	JT1007	JT1007	JT1007	JT1007	JT1007	JT1007	JT1007	JT1007	JT1007	JT1007	JT1007	JT1008	JT1008	JT1008	JT1008	JT1008	JT1008	JT1008	JT1008
mineral	Bt 1 core	Bt 1 core	Bt 1 core	Bt 1 core	Bt 1 rim	Bt 1 rim	Bt 1 rim	Bt 1 rim	Bt 2	Bt 2	Bt 2	Bt 2	Bt 1 core	Bt 1 core	Bt 1	Bt 1	Bt 2	Bt 2	Bt 2	Bt 2
SiO ₂	34.80	34.89	34.82	34.39	34.63	35.03	35.29	34.96	35.56	35.33	35.52	35.09	35.09	35.00	35.53	36.05	36.55	34.97	35.68	32.53
TiO ₂	2.85	2.92	2.67	2.53	2.15	1.57	1.98	2.09	1.56	1.27	1.34	1.68	2.80	2.70	2.60	3.02	2.44	2.70	1.69	12.44
Al ₂ O ₃	17.79	17.89	18.05	17.34	17.23	17.98	17.94	18.02	18.16	17.84	18.58	18.28	18.45	18.56	18.35	17.90	18.32	18.17	17.57	13.23
FeO	25.74	25.96	25.76	25.75	27.10	25.23	25.81	26.35	26.18	25.80	25.85	26.36	24.54	24.45	24.51	24.00	23.21	24.77	25.15	15.64
MnO	0.22	0.25	0.20	0.24	0.32	0.18	0.23	0.21	0.25	0.23	0.20	0.26	0.35	0.32	0.33	0.31	0.33	0.37	0.34	0.09
MgO	5.30	5.74	5.66	5.35	5.73	5.60	5.51	5.65	5.98	6.15	5.58	5.57	6.34	6.37	6.59	6.56	6.54	6.26	7.57	4.16
CaO	0.05	0.01	0.02	0.06	0.02	0.11	0.04	0.03	0.01	0.04	0.04	0.13	0.05	0.05	0.09	0.05	0.03	0.04	0.01	13.17
Na ₂ O	0.10	0.11	0.12	0.98	0.02	1.06	0.05	0.03	0.04	0.02	0.05	0.05	0.11	0.10	0.07	0.08	0.03	0.03	0.00	0.06
K ₂ O	9.47	9.47	9.54	9.51	9.59	9.51	9.35	9.57	9.61	9.58	9.33	9.11	9.34	9.45	9.34	9.45	9.64	9.55	8.92	5.18
Cl	0.04	0.05	0.03	0.46	0.01	0.58	0.05	0.04	0.03	0.03	0.04	0.05	0.04	0.03	0.03	0.04	0.05	0.05	0.07	0.05
F	0.21	0.36	0.44	0.26	0.34	0.16	0.29	0.35	0.11	0.14	0.10	0.10	0.39	0.26	0.35	0.28	0.35	0.38	0.34	1.10
total	96.56	97.81	97.55	96.87	97.17	97.01	96.54	97.31	97.49	96.43	96.63	96.67	97.49	97.29	97.80	97.74	97.49	97.28	97.36	97.72
Si	2.71	2.69	2.70	2.70	2.71	2.73	2.75	2.71	2.74	2.75	2.75	2.73	2.69	2.69	2.71	2.74	2.78	2.70	2.74	2.49
Ti	0.17	0.17	0.16	0.15	0.13	0.09	0.12	0.12	0.09	0.07	0.08	0.10	0.16	0.16	0.15	0.17	0.14	0.16	0.10	0.71
Al	1.63	1.63	1.65	1.60	1.59	1.65	1.64	1.65	1.65	1.64	1.70	1.67	1.67	1.68	1.65	1.60	1.64	1.65	1.59	1.19
Fe	1.68	1.68	1.67	1.69	1.77	1.65	1.68	1.71	1.69	1.68	1.68	1.71	1.58	1.57	1.57	1.53	1.48	1.60	1.62	1.00
Mn	0.01	0.02	0.01	0.02	0.02	0.01	0.01	0.01	0.02	0.02	0.01	0.02	0.02	0.02	0.02	0.02	0.02	0.02	0.02	0.01
Mg	0.62	0.66	0.65	0.63	0.67	0.65	0.64	0.65	0.69	0.71	0.64	0.65	0.73	0.73	0.75	0.74	0.74	0.72	0.87	0.47
Ca	0.00	0.00	0.00	0.00	0.00	0.01	0.00	0.00	0.00	0.00	0.00	0.01	0.00	0.00	0.01	0.00	0.00	0.00	0.00	1.08
Na	0.01	0.02	0.02	0.15	0.00	0.16	0.01	0.01	0.01	0.00	0.01	0.01	0.02	0.01	0.01	0.01	0.00	0.00	0.00	0.01
K	0.94	0.93	0.94	0.95	0.96	0.95	0.93	0.95	0.94	0.95	0.92	0.90	0.91	0.93	0.91	0.92	0.93	0.94	0.87	0.50
Cl	0.00	0.00	0.00	0.04	0.00	0.05	0.00	0.00	0.00	0.00	0.00	0.00	0.00	0.00	0.00	0.00	0.00	0.00	0.01	0.00
F	0.03	0.05	0.06	0.04	0.05	0.02	0.04	0.05	0.01	0.02	0.01	0.01	0.05	0.03	0.05	0.04	0.05	0.05	0.04	0.14
Sum cations	7.78	7.80	7.80	7.90	7.85	7.90	7.78	7.82	7.82	7.83	7.79	7.79	7.78	7.79	7.77	7.75	7.73	7.79	7.81	7.46
Mg/(Mg+Fe)	0.27	0.28	0.28	0.27	0.27	0.28	0.28	0.28	0.29	0.30	0.28	0.27	0.32	0.32	0.32	0.33	0.33	0.31	0.35	0.32
Cl/K	0.00	0.00	0.00	0.04	0.00	0.06	0.01	0.00	0.00	0.00	0.00	0.00	0.06	0.04	0.05	0.04	0.05	0.05	0.05	0.29

Table 2

Sample	JT1007	JT1007	JT1007	JT1007	JT1008	JT1008	JT1008	JT1008	JT1008	JT1008	JT1008	JT1008	JT1008	JT1008	JT1008	JT1008	JT1008
Mineral	Alpine Wm	Alpine Wm	Alpine Wm	Alpine Wm	large Wm1	large Wm1	large Wm1	large Wm1	small Wm1	small Wm1	epitactic Wm2	epitactic Wm2	Wm2 on Bt1	Wm2 on Bt1	Wm2 on Bt1	Wm3	Wm3
SiO ₂	47.58	47.60	47.53	46.91	46.64	46.43	46.57	46.59	45.97	46.15	46.93	47.48	47.91	48.05	46.76	46.40	47.09
TiO ₂	0.32	0.38	0.52	0.25	0.57	0.58	0.48	0.60	0.79	2.30	1.12	0.71	2.17	1.77	1.97	0.97	1.80
Al ₂ O ₃	32.47	32.40	33.14	34.23	36.26	36.29	36.19	36.05	35.39	33.61	33.61	32.98	29.07	31.28	31.81	33.98	31.96
FeO	2.94	3.03	2.61	2.36	1.07	1.09	1.01	1.28	1.26	1.75	1.72	2.10	3.66	2.22	2.71	2.69	3.13
MnO	0.00	0.01	0.01	0.04	0.00	0.08	0.00	0.00	0.04	0.01	0.09	0.05	0.07	0.01	0.00	0.01	0.07
MgO	1.22	1.22	1.22	0.86	0.50	0.55	0.52	0.61	0.56	0.75	1.04	1.17	1.87	1.44	1.25	0.89	1.26
CaO	0.04	0.03	0.04	0.04	0.05	0.01	0.03	0.07	0.03	0.02	0.04	0.08	0.03	0.01	0.01	0.02	0.01
Na ₂ O	0.20	0.24	0.27	0.26	0.80	0.84	0.45	0.35	0.40	0.28	0.29	0.27	0.11	0.22	0.23	0.21	0.25
K ₂ O	10.98	11.09	10.98	10.92	10.20	10.10	10.70	10.78	10.90	10.92	10.79	10.73	10.85	10.99	10.96	11.00	10.89
Cl	0.00	0.01	0.00	0.01	0.00	0.01	0.00	0.00	0.00	0.01	0.00	0.00	0.00	0.00	0.00	0.01	0.01
F	0.00	0.00	0.00	0.00	0.00	0.00	0.00	0.00	0.00	0.00	0.00	0.00	0.00	0.00	0.00	0.00	0.00
Total	95.74	96.01	96.33	95.89	96.09	95.97	95.95	96.34	95.33	95.80	95.62	95.58	95.75	95.99	95.70	96.18	96.47
Si	3.18	3.18	3.15	3.12	3.07	3.06	3.07	3.07	3.07	3.08	3.12	3.16	3.22	3.20	3.14	3.09	3.14
Ti	0.02	0.02	0.03	0.01	0.03	0.03	0.02	0.03	0.04	0.12	0.06	0.04	0.11	0.09	0.10	0.05	0.09
Al	2.56	2.55	2.59	2.68	2.81	2.82	2.81	2.80	2.78	2.64	2.64	2.59	2.31	2.45	2.51	2.67	2.51
Fe	0.16	0.17	0.14	0.13	0.06	0.06	0.06	0.07	0.07	0.10	0.10	0.12	0.21	0.12	0.15	0.15	0.17
Mn	0.00	0.00	0.00	0.00	0.00	0.00	0.00	0.00	0.00	0.00	0.01	0.00	0.00	0.00	0.00	0.00	0.00
Mg	0.12	0.12	0.12	0.09	0.05	0.05	0.05	0.06	0.06	0.07	0.10	0.12	0.19	0.14	0.12	0.09	0.13
Ca	0.00	0.00	0.00	0.00	0.00	0.00	0.00	0.01	0.00	0.00	0.00	0.01	0.00	0.00	0.00	0.00	0.00
Na	0.03	0.03	0.03	0.03	0.10	0.11	0.06	0.04	0.05	0.04	0.04	0.03	0.01	0.03	0.03	0.03	0.03
K	0.94	0.94	0.93	0.93	0.86	0.85	0.90	0.91	0.93	0.93	0.92	0.91	0.93	0.93	0.94	0.93	0.93
Cl	0.00	0.00	0.00	0.00	0.00	0.00	0.00	0.00	0.00	0.00	0.00	0.00	0.00	0.00	0.00	0.00	0.00
F	0.00	0.00	0.00	0.00	0.00	0.00	0.00	0.00	0.00	0.00	0.00	0.00	0.00	0.00	0.00	0.00	0.00
Sum cations	7.01	7.02	7.01	7.00	6.98	6.98	6.98	6.98	6.99	6.97	6.98	6.98	6.99	6.97	6.99	7.01	7.00
Mg/(Mg+Fe)	0.42	0.42	0.45	0.39	0.45	0.47	0.48	0.46	0.44	0.43	0.52	0.50	0.48	0.54	0.45	0.37	0.42
Na/(Na+K)	0.03	0.03	0.04	0.04	0.11	0.11	0.06	0.05	0.05	0.04	0.04	0.04	0.02	0.03	0.03	0.03	0.03

Table 3

No.	mineral	laser	IR # shots	³⁶ Ar _(atm)	±2σ	³⁷ Ar _(Ca)	±2σ	³⁸ Ar _(Ci)	±2σ	³⁹ Ar _(K)	±2σ	⁴⁰ Ar _(tot)	±2σ	Age	±2σ	⁴⁰ Ar* %	type
UV (μm ²)														(Ma)			
JT1008, I=0.0055482±0.0000344																	
121A	Bt	IR	2	3.5E-05	4.0E-05	5.9E-04	8.4E-04	3.3E-04	7.6E-05	3.9E-02	2.4E-04	1.5E-01	5.8E-04	35.9	3.0	92.9	thick section A
121C	Bt+Wm	IR	2	2.6E-05	4.3E-05	—	—	4.1E-04	9.9E-05	6.3E-02	3.6E-04	2.8E-01	1.2E-03	43.3	2.0	97.1	thick section A
121D	Bt+Wm	IR	3	1.7E-04	4.0E-05	4.9E-04	8.8E-04	4.6E-04	9.8E-05	4.8E-02	2.3E-04	2.5E-01	6.6E-04	40.3	2.4	79.5	thick section A
121E	Bt	IR	2	2.3E-05	4.0E-05	2.2E-04	9.2E-04	5.8E-04	1.3E-04	6.5E-02	3.6E-04	2.4E-01	5.7E-04	35.6	1.8	97.0	thick section A
121G	Bt	IR	4	1.7E-05	3.8E-05	2.4E-04	7.6E-04	1.0E-03	1.9E-04	1.0E-01	4.9E-04	3.8E-01	8.0E-04	35.9	1.1	98.4	thick section A
121H	Bt	IR	4	5.4E-05	3.5E-05	2.4E-03	1.2E-03	7.9E-04	1.5E-04	8.5E-02	4.6E-04	3.2E-01	7.7E-04	35.7	1.2	94.8	thick section A
121J	Bt	IR	3	3.5E-05	3.2E-05	1.2E-04	7.1E-04	6.8E-04	1.3E-04	7.3E-02	4.0E-04	2.6E-01	7.1E-04	34.5	1.3	95.8	thick section A
144B	Bt	IR	2	1.9E-04	4.5E-05	5.0E-04	2.7E-03	4.5E-04	9.3E-05	5.2E-02	4.3E-04	2.4E-01	3.1E-03	35.5	2.6	76.2	thick section B
144C	Bt	IR	4	1.8E-04	2.9E-05	8.5E-04	2.6E-03	4.3E-04	8.8E-05	5.3E-02	3.2E-04	2.4E-01	3.2E-03	35.1	1.7	77.5	thick section B
144D	Bt	IR	4	1.0E-04	2.8E-05	1.9E-03	3.3E-03	6.4E-04	1.4E-04	6.0E-02	4.2E-04	2.4E-01	3.2E-03	35.1	1.5	87.4	thick section B
144F	Bt	IR	3	3.0E-05	3.1E-05	1.1E-03	3.1E-03	3.4E-04	8.3E-05	3.9E-02	3.1E-04	1.5E-01	3.1E-03	35.1	2.4	93.9	thick section B
144G	Bt	IR	3	2.1E-05	2.9E-05	1.6E-03	2.8E-03	4.8E-04	1.1E-04	5.3E-02	2.9E-04	2.0E-01	3.1E-03	37.0	1.7	96.8	thick section B
121N	Bt+Wm	UV	100x300	1.8E-04	3.0E-05	2.2E-04	8.2E-04	3.3E-04	8.7E-05	6.0E-02	3.8E-04	2.7E-01	1.3E-03	36.7	1.5	80.5	thick section A
121O	Wm	UV	100x300	2.0E-05	3.3E-05	7.1E-05	1.0E-03	1.3E-04	7.1E-05	6.0E-02	3.0E-04	2.7E-01	1.1E-03	43.8	1.6	97.6	thick section A
121Q	Wm2+Bt2	UV	100x300	6.4E-05	2.7E-05	4.6E-04	1.2E-03	3.0E-05	6.9E-05	6.4E-02	3.7E-04	2.8E-01	1.1E-03	40.8	1.2	93.1	thick section A
121R	Wm2+Bt2	UV	100x300	4.3E-05	5.6E-05	5.0E-04	9.6E-04	6.4E-05	6.5E-05	6.7E-02	3.8E-04	2.5E-01	1.0E-03	34.8	2.4	94.6	thick section A
121U	Wm	UV	100x300	7.8E-05	4.4E-05	2.3E-04	7.6E-04	3.0E-05	5.9E-05	3.8E-02	3.0E-04	5.3E-01	1.2E-03	128.2	3.3	95.6	thick section A
121V	Wm	UV	150x200	5.0E-05	6.3E-05	1.9E-04	7.8E-04	0.0E+00	0.0E+00	4.6E-02	2.8E-04	2.3E-01	5.8E-04	46.1	4.0	93.4	thick section A
121W	Wm	UV	100x300	1.1E-04	3.3E-05	6.4E-05	6.6E-04	4.7E-05	5.9E-05	4.7E-02	2.5E-04	2.3E-01	7.1E-04	41.7	2.0	85.8	thick section A
121X	Wm	UV	100x300	8.6E-05	3.4E-05	1.2E-04	7.2E-04	4.5E-05	6.7E-05	5.6E-02	3.7E-04	4.3E-01	7.8E-04	69.6	1.8	93.9	thick section A
121Y	Wm	UV	100x300	6.0E-05	3.0E-05	1.7E-04	1.0E-03	2.5E-05	7.6E-05	5.7E-02	4.2E-04	2.9E-01	1.0E-03	47.0	1.6	93.7	thick section A
121Z	Wm	UV	100x270	8.2E-04	3.2E-05	3.4E-04	8.9E-04	0.0E+00	0.0E+00	5.4E-02	3.5E-04	6.8E-01	1.4E-03	79.3	1.8	64.2	thick section A
122A	Wm	UV	100x270	2.3E-05	3.9E-05	3.8E-04	8.6E-04	1.3E-05	6.6E-05	4.3E-02	3.8E-04	2.3E-01	9.8E-04	50.1	2.6	96.8	thick section A
JT1008, I=0.0027175±0.0000174																	
12M0019B	Wm	CO2	1	9.6E-04	2.9E+00	2.5E-03	1.9E+03	7.5E-06	5.5E+02	8.9E-02	2.5E-01	1.6E+00	5.1E-01	85.5	1.0	84.9	single crystal separate
12M0019C	Wm	CO2	1	6.1E-04	2.5E+00	2.5E-03	1.9E+03	5.1E-05	1.1E+02	1.1E-01	2.9E-01	2.0E+00	2.3E-01	86.7	0.6	91.7	single crystal separate
12M0019D	Wm	CO2	1	2.4E-04	6.4E+00	-2.8E-03	1.7E+03	0.0E+00	0.0E+00	8.1E-02	2.1E-01	1.7E+00	2.7E-01	102.7	0.7	96.1	single crystal separate
12M0019G	Wm	CO2	1	2.5E-04	7.0E+00	9.3E-03	3.3E+02	9.5E-05	6.1E+01	1.0E-01	3.4E-01	1.9E+00	2.8E-01	89.6	0.8	96.2	single crystal separate
12M0019H	Wm	CO2	1	6.4E-04	3.1E+00	1.4E-02	2.3E+02	0.0E+00	0.0E+00	4.8E-01	1.7E-01	8.2E+00	7.9E-02	82.2	0.3	97.7	single crystal separate
12M0027A	Wm	CO2	1	3.1E-04	6.7E+00	5.1E-03	7.7E+02	5.3E-06	4.4E+02	4.5E-02	2.4E-01	1.9E+00	3.2E-01	199.5	1.5	95.5	single crystal separate
12M0027B	Wm	CO2	1	2.7E-04	6.8E+00	4.5E-03	1.0E+03	0.0E+00	0.0E+00	2.8E-02	4.0E-01	1.3E+00	4.2E-01	217.8	2.4	94.4	single crystal separate
12M0027C	Wm	CO2	1	4.4E-05	2.7E+01	5.3E-03	5.6E+02	1.0E-05	1.9E+02	1.5E-02	5.4E-01	1.6E-01	2.2E+00	53.6	2.3	92.6	single crystal separate
12M0027E	Wm	CO2	1	5.3E-04	4.0E+00	6.9E-03	4.3E+02	3.2E-05	8.5E+01	5.1E-02	3.5E-01	2.4E+00	2.8E-01	215.3	1.8	93.7	single crystal separate
12M0027F	Wm	CO2	1	1.3E-04	1.1E+01	5.3E-03	6.5E+02	2.8E-05	1.0E+02	6.2E-02	2.3E-01	1.2E+00	3.6E-01	93.6	0.8	96.8	single crystal separate
12M0027G	Wm	CO2	1	2.6E-04	5.8E+00	-2.2E-03	1.6E+03	4.9E-06	6.7E+02	5.6E-02	3.2E-01	2.1E+00	2.6E-01	171.6	1.3	96.4	single crystal separate
12M0027J	Wm	CO2	1	9.6E-04	2.4E+00	-1.5E-02	2.4E+02	1.6E-05	3.3E+02	1.2E-01	2.4E-01	2.7E+00	2.7E-01	105.7	0.7	90.3	single crystal separate
12M0027K	Wm	CO2	1	1.1E-03	2.0E+00	2.3E-03	1.3E+03	5.7E-05	3.7E+02	5.5E-01	2.6E-01	1.6E+01	2.4E-01	133.9	0.9	97.9	single crystal separate
12M0028A	Wm	CO2	1	1.1E-04	1.0E+01	6.2E-03	4.2E+02	3.2E-05	7.8E+01	5.8E-02	2.2E-01	2.6E+00	1.4E-01	204.5	1.0	98.7	single crystal separate
12M0028B	Wm	CO2	1	2.8E-04	8.6E+00	1.4E-02	2.5E+02	5.2E-05	1.0E+02	1.3E-01	2.7E-01	3.4E+00	2.5E-01	128.9	0.9	97.6	single crystal separate
12M0028C	Wm	CO2	1	5.0E-05	2.4E+01	4.6E-03	6.2E+02	0.0E+00	0.0E+00	2.3E-02	5.6E-01	8.4E-01	4.4E-01	171.8	2.3	98.2	single crystal separate
12M0028D	Wm	CO2	1	4.1E-05	3.6E+01	-4.1E-03	7.4E+02	0.0E+00	0.0E+00	6.1E-02	5.1E-01	1.5E+00	2.9E-01	120.3	1.4	99.2	single crystal separate
12M0028F	Wm	CO2	1	1.5E-04	8.4E+00	-1.3E-02	1.8E+02	0.0E+00	0.0E+00	6.0E-02	2.7E-01	1.4E+00	2.8E-01	109.0	0.8	96.9	single crystal separate
12M0028G	Wm	CO2	1	6.9E-04	3.9E+00	1.0E-02	4.3E+02	2.9E-04	7.8E+01	5.7E-01	1.6E-01	1.7E+01	6.6E-02	141.6	0.5	98.8	single crystal separate
JT1007, I=0.0027302±0.0000164																	
11M0124B	Bt	IR (12W)	3	5.2E-05	2.5E+01	7.4E-03	5.6E+01	1.3E-03	2.1E+00	6.7E-02	3.4E-01	6.2E-01	1.6E-01	44.5	0.6	97.5	single crystal separate
11M0124C	Bt	IR (12W)	5	3.5E-05	3.5E+01	1.2E-03	4.4E+02	1.0E-03	2.3E+00	4.8E-02	3.2E-01	4.7E-01	1.1E-01	46.5	0.8	97.7	single crystal separate
11M0124E	Bt	IR (12W)	3	4.0E-05	2.8E+01	6.3E-03	8.6E+01	1.1E-03	2.0E+00	6.1E-02	3.6E-01	6.3E-01	8.1E-02	49.2	0.6	98.1	single crystal separate
11M0124F	Bt	IR (12W)	5	4.3E-05	2.8E+01	4.9E-03	8.8E+01	1.3E-03	1.5E+00	6.0E-02	3.4E-01	6.5E-01	6.6E-02	51.4	0.7	98.0	single crystal separate
11M0125A	Bt	IR (12W)	4	1.5E-05	7.1E+01	-3.1E-03	1.3E+02	5.8E-04	5.2E+00	3.2E-02	3.1E-01	4.5E-01	1.0E-01	66.1	1.0	98.9	single crystal separate
11M0125C	Bt	IR (12W)	5	3.8E-05	3.1E+01	1.9E-03	2.4E+02	1.1E-03	3.4E+00	5.3E-02	3.7E-01	5.2E-01	1.8E-01	46.7	0.7	97.8	single crystal separate
11M0125D	Bt	IR (12W)	3	1.3E-05	9.2E+01	-9.9E-04	4.2E+02	8.2E-04	3.4E+00	4.6E-02	3.1E-01	5.7E-01	8.0E-02	59.3	0.8	99.2	single crystal separate
11M0125E	Bt	IR (12W)	5	5.0E-05	3.5E+01	3.3E-03	1.0E+02	1.1E-03	1.9E+00	5.7E-02	3.8E-01	5.8E-01	1.6E-01	48.2	0.9	97.4	single crystal separate
11M0125H	Bt	IR (12W)	3	6.1E-05	2.5E+01	5.4E-03	9.6E+01	8.9E-04	2.8E+00	4.5E-02	4.2E-01	5.5E-01	1.1E-01	56.6	1.1	96.6	single crystal separate
11M0125I	Bt	IR (12W)	5	7.3E-05	2.2E+01	2.3E-03	2.2E+02	7.8E-04	3.9E+00	4.1E-02	5.6E-01	4.4E-01	2.1E-01	49.8	1.3	95.1	single crystal separate
11M0125M	Bt	IR (12W)	3	3.6E-05	3.1E+01	-9.4E-04	4.8E+02	7.2E-04	1.7E+00	3.9E-02	3.9E-01	3.7E-01	1.8E-01	45.2	0.9	97.0	single crystal separate
11M0125N	Bt	IR (12W)	2	4.0E-04	3.8E+00	1.2E-02	5.4E+01	4.0E-03	7.7E-01	2.1E-01	3.0E-01	2.8E+00					

Figure 1

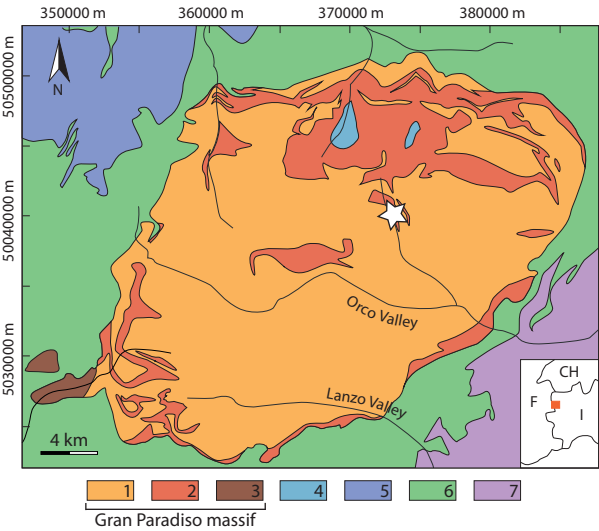


Figure 2

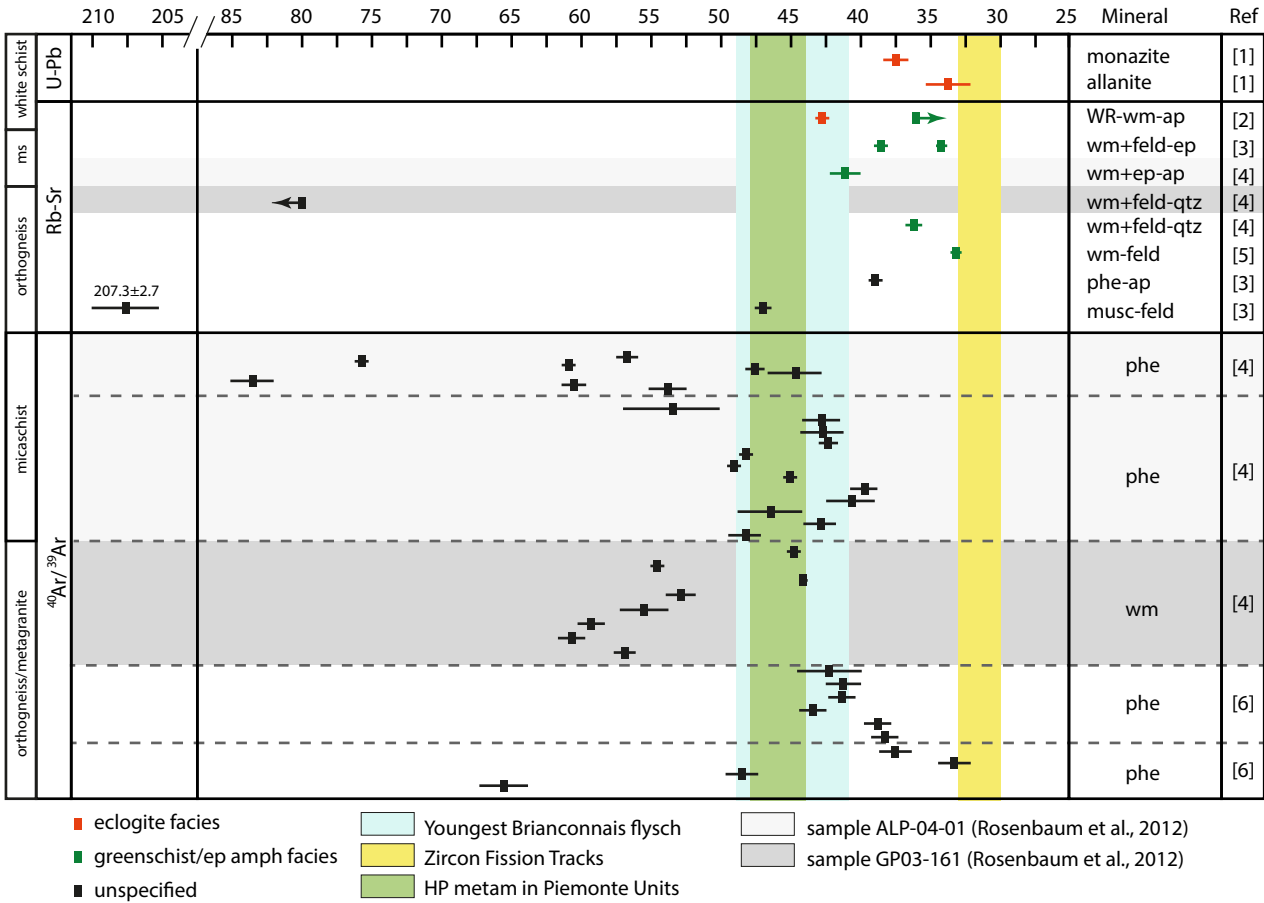


Figure 3

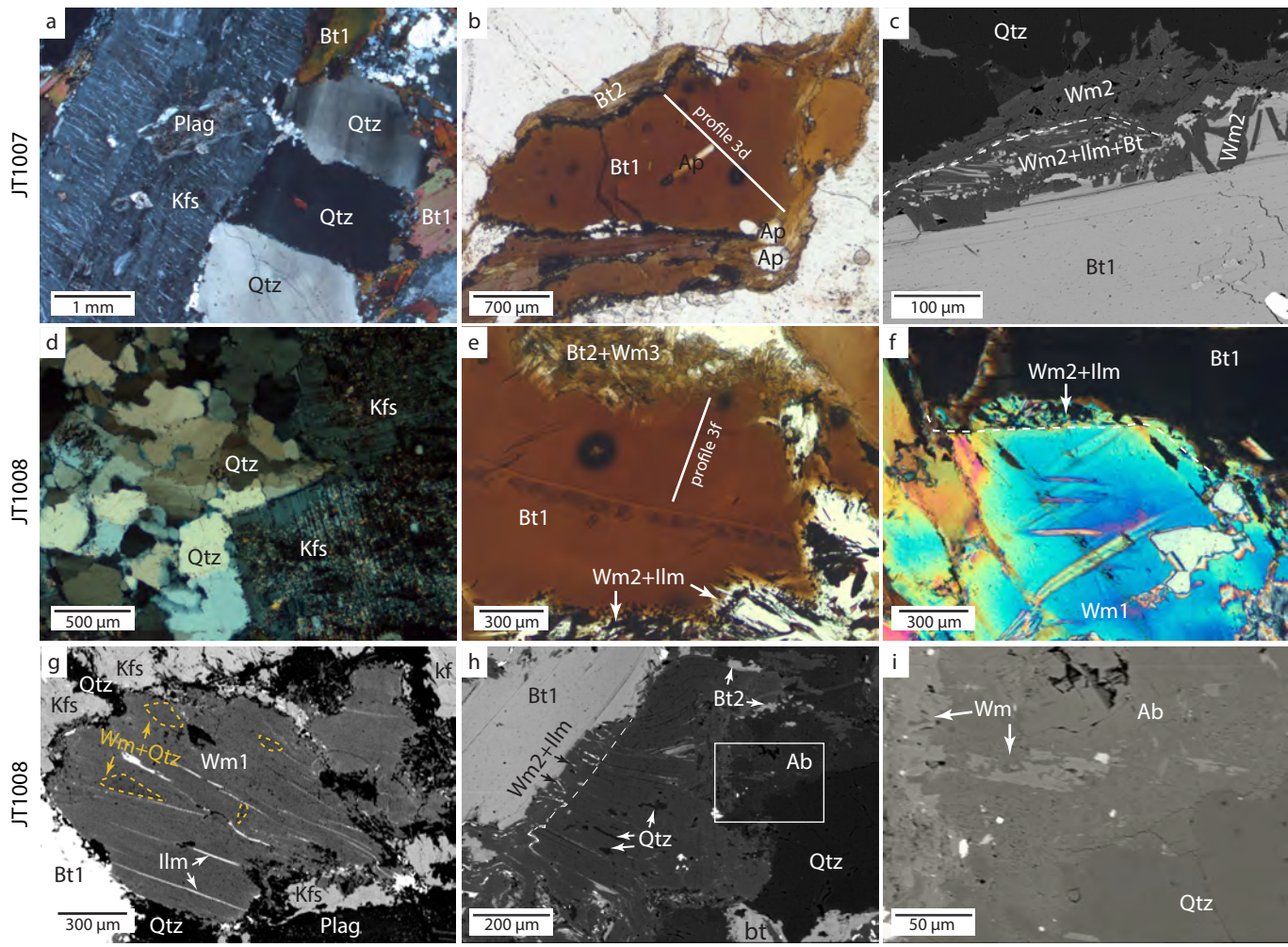


Figure 4

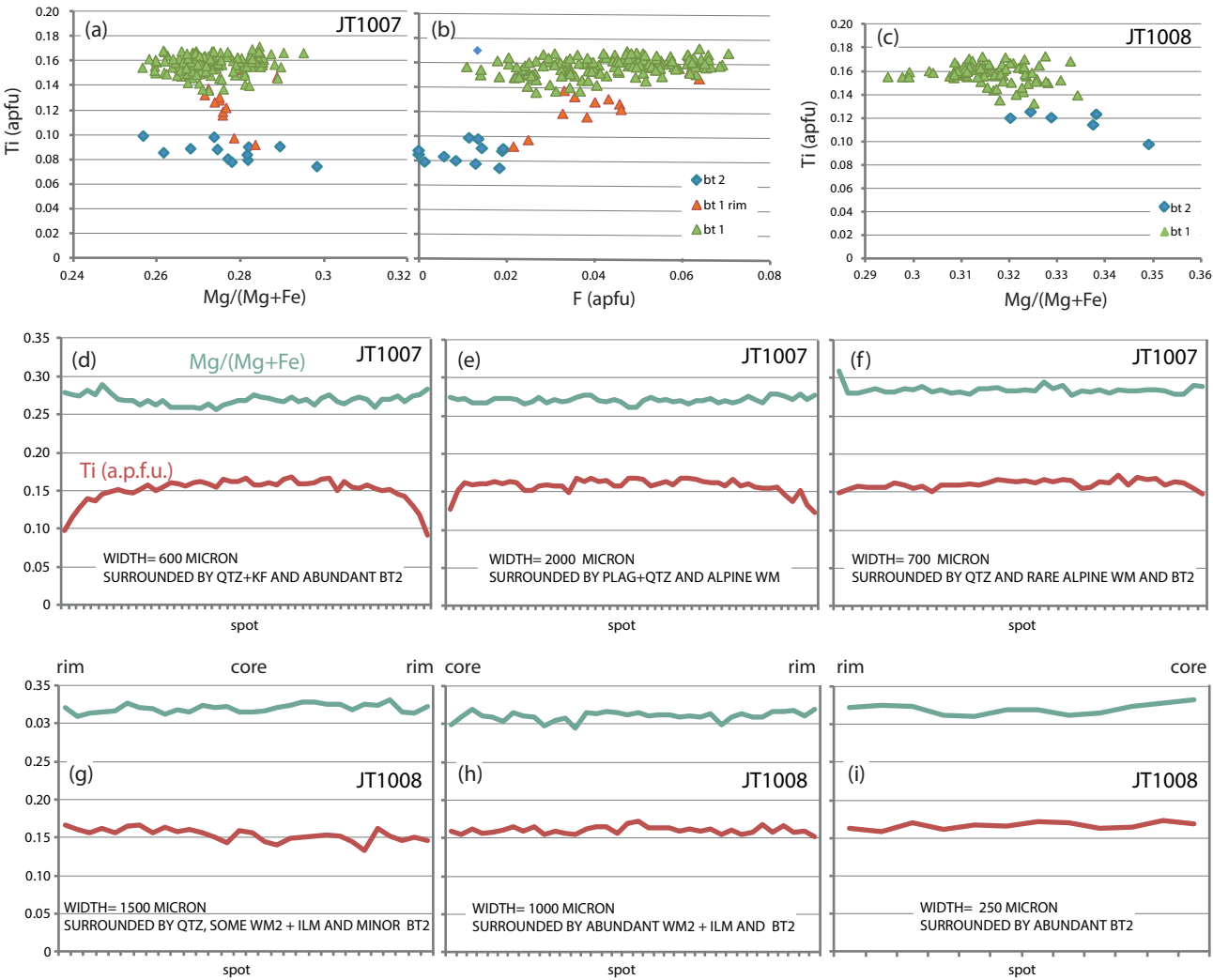


Figure 5

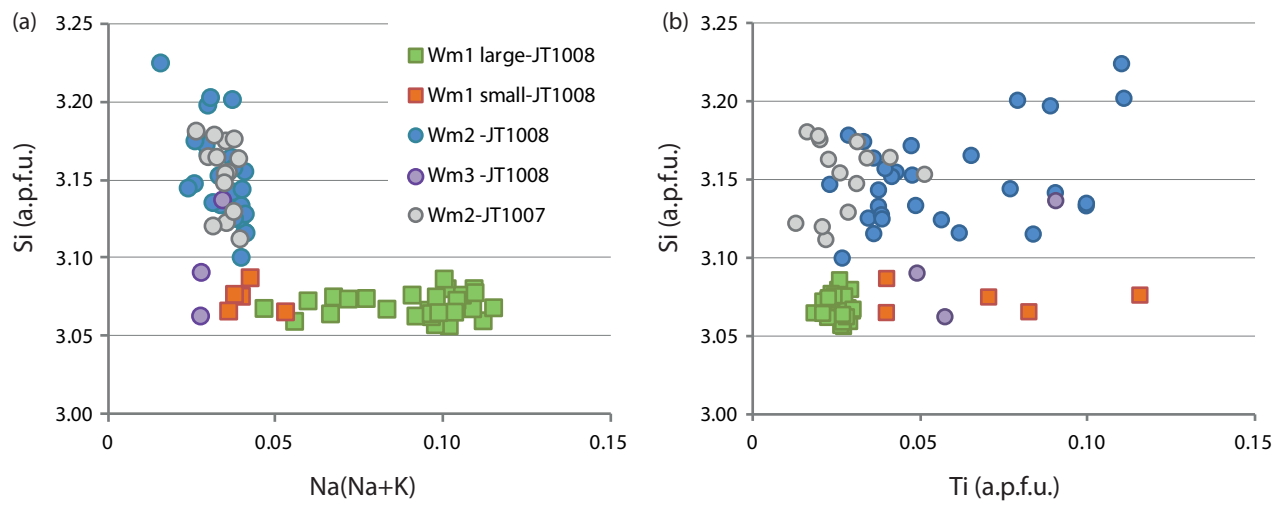


Figure 6

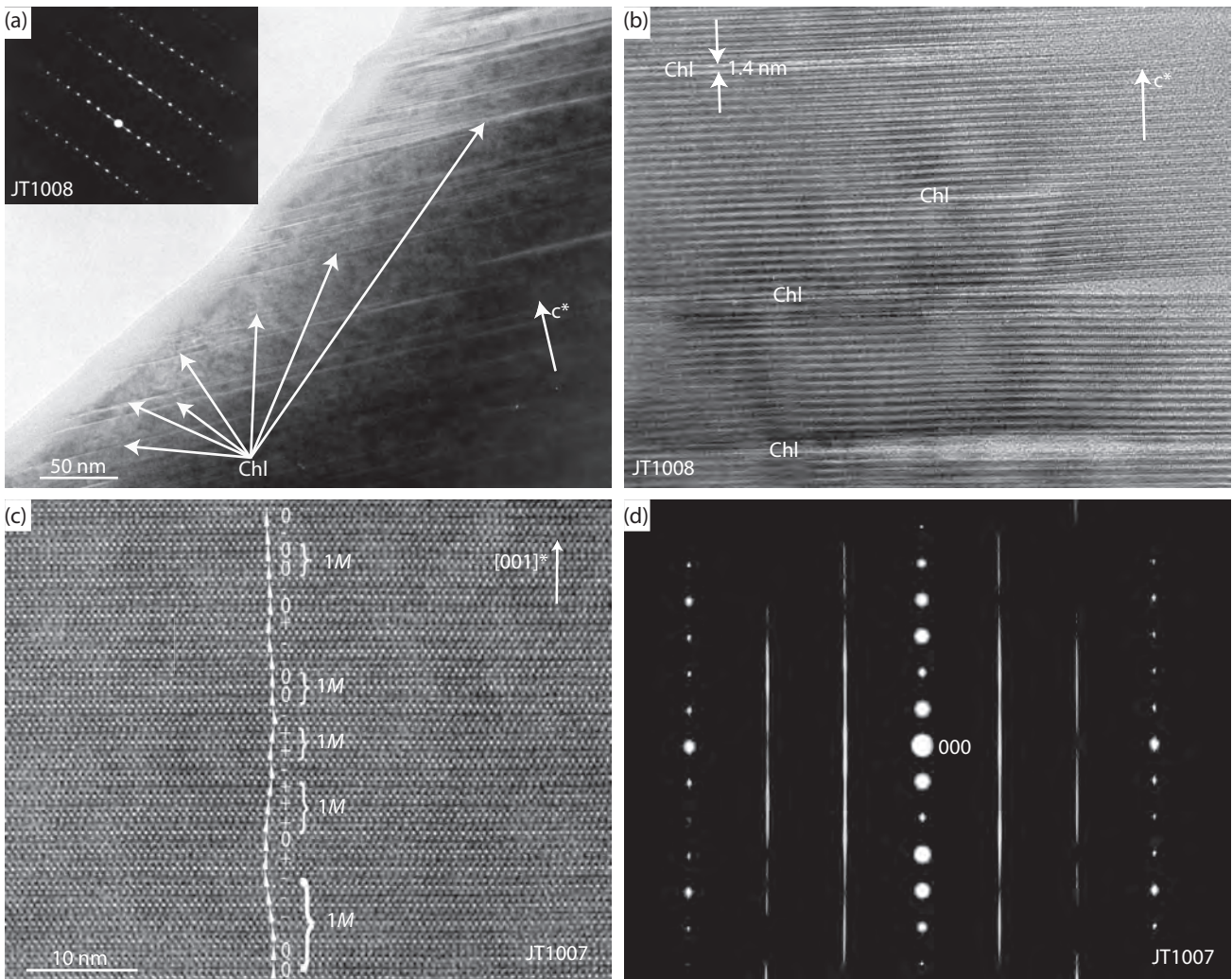


Figure 7

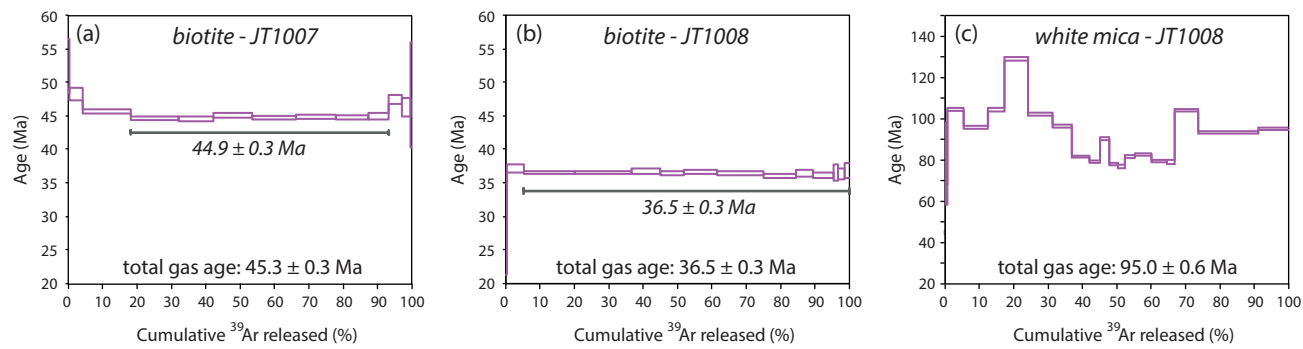


Figure 8

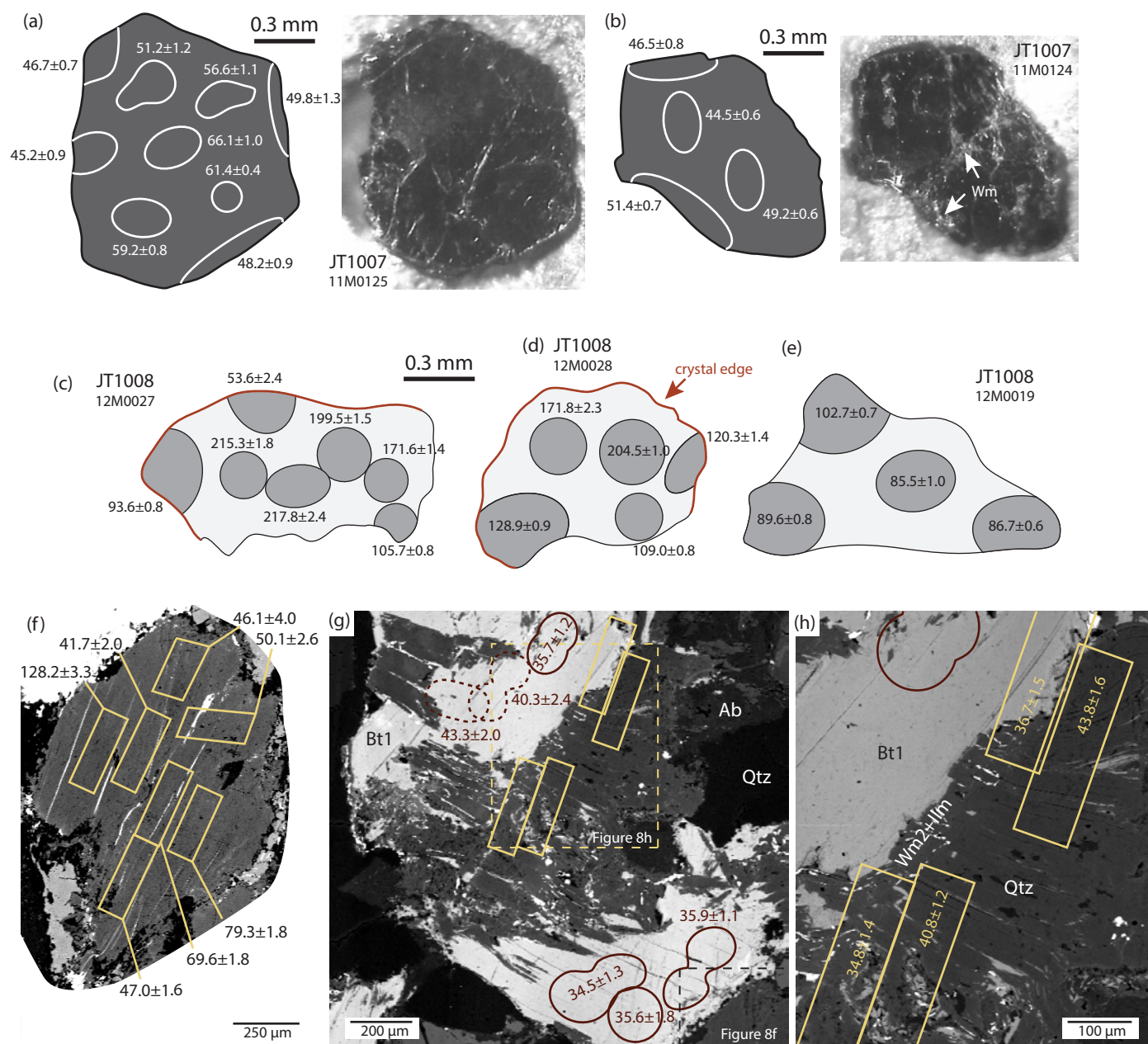


Figure 9

